Title:
A stochastic pooling motif mediates information transfer from receptor assemblies into NF-κB

Authors:
J. Agustin Cruz[1,3], Chaitanya S. Mokashi[1,3], Gabriel J. Kowalczyk[1], Yue Guo[1,2], Qiuhong Zhang[1], Sanjana Gupta[1], David L. Schipper[1], Robin E. C. Lee[1,*]

Affiliations:
[1] Department of Computational and Systems Biology, School of Medicine, University of Pittsburgh, Pittsburgh, PA 15213, USA
[2] Department of Physics and Astronomy, University of Pittsburgh, Pittsburgh, PA 15260, USA
[3] These authors contributed equally
[*] Correspondence: RobinLee@pitt.edu

Summary:

A myriad of inflammatory cytokines regulate signaling pathways to maintain cellular homeostasis. The IKK complex is an integration hub for cytokines that govern NF-κB signaling. In response to inflammation, IKK is activated through recruitment to receptor-associated protein assemblies. How and what information IKK complexes transmit about the milieu are open questions. Here we track dynamics of IKK complexes and nuclear NF-κB to identify upstream signaling features that determine same-cell responses. Experiments and modeling of single complexes reveals their size, number, and timing relays cytokine-specific control over shared signaling mechanisms with feedback regulation that is independent of transcription. Our results provide evidence for variable-gain stochastic pooling, a noise-reducing motif that enables cytokine-specific regulation and parsimonious information transfer. We propose that emergent properties of stochastic pooling are general principles of receptor signaling that have evolved for constructive information transmission in noisy molecular environments.

Main Text:

Introduction:

A limited number of transmembrane receptors expressed on the cell surface mediate crucial transmission of information between extracellular and intracellular signaling molecules. Key questions are understanding the mechanisms and limitations that underlie signal transmission, in particular for cytokine receptor signaling that is often deregulated in disease. The nuclear-factor kappa-B (NF-κB) signaling pathway is an archetypal molecular communication channel that transmits information about extracellular cytokines to regulate cellular adaptation through activation of the RelA transcription factor (Cheong et al., 2011; Selimkhanov et al., 2014; Zhang et al., 2017). When ligated with inflammatory molecules, such as tumor necrosis factor (TNF), interleukin-1-β (IL-1), among others, many activated receptors converge on NF-κB signaling (Aggarwal, 2003; Hayden and Ghosh, 2008).

Ligation of TNF to the TNF receptor (TNFR1) recruits adaptor proteins and enzymes to form a large multiprotein complex near the plasma membrane (Besse et al., 2007; Jackson-Bernitsas et al., 2007; Lim et al., 2017; Micheau and Tschopp, 2003). Ubiquitin modifying enzymes are critical components that assemble linear, branched, and mixed polyubiquitin scaffolds around the multiprotein complex (Clague et al., 2019; Ikeda et al., 2011; Komander and Rape, 2012; Wertz et al., 2004). The NEMO subunit of the cytoplasmic IκB-kinase (IKK) complex is rapidly recruited via direct interaction with the polyubiquitin scaffold and accessory proteins, where IKK is activated through induced proximity with regulatory kinases (Clark et al., 2013; Ea et al., 2006; Haas et al., 2009; Hayden and Ghosh, 2008). The fully assembled TNFR1 complex, referred to as ‘Complex

I' (CI; (Micheau and Tschopp, 2003)), is a master regulator of inflammation-dependent NF-κB signaling. Although other inflammatory molecules such as IL-1 signal through CI-like complexes using different receptors, adaptor proteins (Ahmad et al., 2007; Lin et al., 2010), and varying compositions of ubiquitin chain scaffolds (Scholefield et al., 2016; Tarantino et al., 2014), all regulate NF-κB through IKK activation mediated by induced-proximity with other signaling mediators that reside on CI (Hinz and Scheidereit, 2014).

When observed in single cells exposed to inflammatory stimuli, the RelA subunit of NF-κB encodes a dynamic transcriptional signal by translocating from the cytoplasm into the nucleus (Ashall et al., 2009; Lee et al., 2014; Nelson et al., 2004; Selimkhanov et al., 2014; Zhang et al., 2017). Models calibrated to single-cell RelA data (Ashall et al., 2009; Hoffmann et al., 2002; Lee et al., 2014; Werner et al., 2005) have revealed numerous transcriptional mechanisms and emergent properties that place the NF-κB pathway among exemplars of dynamical biological systems (Alon, 2007; Purvis and Lahav, 2013). Key to these findings are two mediators of negative feedback, IκBα and A20, which are transcriptionally regulated by NF-κB. IκBα restores NF-κB to its baseline cytoplasmic localization through nuclear export and sequestration, whereas A20 diminishes kinase activation upstream of NF-κB through disassembly of CI-like structures in addition to non-catalytic mechanisms (Ashall et al., 2009; Hoffmann et al., 2002; Skaug et al., 2011; Werner et al., 2005; Wertz et al., 2004). Dynamical regulation of transcription and feedback via NF-κB is strongly recapitulated between models and experiments; however, there is a dearth of quantitative single-cell data at the level of cytokine detection and dynamical properties of CI-like complexes to substantiate our understanding of upstream signal transmission.

Here, we develop genetically modified cells that endogenously express fluorescent protein fusions of NEMO and RelA, allowing same-cell measurements of CI-like structures and canonical NF-kB signaling from live-cell images. We establish differences between TNF and IL1 responses in biophysical properties of NEMO complexes and demonstrate a continuum relating CI-like structures and downstream NF-kB responses in the same cell. By tracking single complexes, we demonstrate that: i) cytokine dosage and time-varying presentation modulates the timing and numbers of CI-like structures; ii) single complexes have switch-like activation profiles where the aggregate of NEMO recruitment and time-varying properties of each complex are cytokine-specific; and, iii) that dynamics of formation and dissolution for single complexes during the primary cytokine response are independent of transcriptional feedback. Finally, we characterize a signaling motif called a variable-gain stochastic pooling network (SPN) that encompasses our experimental observations. The variable-gain SPN motif has beneficial noise-mitigation properties and provides a trade-off between information fidelity, ligand specificity, and resource allocation for intracellular signaling molecules. We propose that the variable-gain SPN architecture, and its associated benefits to signal transmission, are common mechanisms for receptor-mediated signal transduction.

Results:

Surface receptor expression is limiting for numbers of cytokine-induced signaling complexes.

IKK activity is a convergence point for pro-inflammatory signals that regulate NF-κB downstream of many cytokine receptors (Pahl, 1999; Werner et al., 2005). Ligands that bind to multiple receptors with differing kinetics (MacEwan, 2002), and decoy receptors that sequester or antagonize signaling complexes (Neumann et al., 2000), layer additional complexity to signal initiation at the plasma membrane. To establish expectations for numbers and types of IKK-activating complexes, we measured surface receptor expression in U2OS cells that were previously shown to form dynamic IKK puncta in response to TNF and IL-1 (Pabon et al., 2019; Tarantino et al., 2014). Using flow cytometry with reference beads for absolute quantification, we estimated the number of surface receptors per cell for TNFR1, TNFR2, IL-1R1, IL-1R2, and IL1-R3 (Figures 1 & S1). On average, each U2OS cell presented approximately 1300 TNFR1, 700 IL-1R1, and an abundance of IL-1R3 surface receptors. Only a small number of TNFR2 and IL-1R2 were detected on the cell surface. For reference, we measured surface receptors on HeLa and KYM1 cells (Figure S1) and found results consistent with previous reports for TNFRs (Jupp et al., 2001; Lehmann and Droge, 1986; Watanabe et al., 1988), and agreement with surface receptor expression in other cell lines (Dower et al., 1985; Karathanasis et al., 2020; Kull et al., 1985; Rubin et al., 1985)

Although activated TNFR1 and TNFR2 both form TNF-induced homotrimeric complexes, the TNFR2 subtype binds with lower affinity to soluble TNF and shows enhanced activation by membrane-bound TNF (Grell et al., 1998; MacEwan, 2002). In

contrast, ligand-activated IL-1 receptor (IL-1R1) forms a heterodimer with the IL-1R3 accessory protein and dimerization can be inhibited through competitive sequestration by the IL-1R2 decoy (Neumann et al., 2000) (Figure 1A). Because surface expression of TNFR2 and IL-1R2 are comparably low in U2OS, receptor composition of TNF and IL-1-induced oligomers will consist predominantly of TNFR1 trimers and IL-1R1-1R3 respectively. Together with known receptor-ligand stoichiometry (Figure 1A), our results predict that single cells can simultaneously form a maximum of hundreds of IKK-recruiting complexes for saturating cytokine concentrations (approximately 400 and 700 for TNF and IL-1 respectively). Remarkably, surface receptor expression is significantly lower than numbers for downstream signaling molecules such as NEMO that are expressed in orders of a million per cell (Hwang et al., 2015).

Cytokine-specific and dose-specific modulation of NEMO complex features.

We set out to investigate how cytokine receptors engage NEMO as an integration hub to regulate NF-κB signaling. To counteract effects of NEMO overexpression, which can significantly inhibit NF-κB activation (Figure S2, and (Hwang et al., 2015)), we used CRISPR/Cas9 for targeted insertion of coding sequences for fluorescent proteins into the U2OS cell line. The resulting cells co-express N-terminal fusions of EGFP-NEMO and mCh-RelA from their endogenous loci which can be used to monitor dynamic signaling events by live-cell imaging (Pabon et al., 2019).

In response to TNF or IL-1, EGFP-NEMO transiently localizes to punctate structures near the plasma membrane (Pabon et al., 2019; Scholefield et al., 2016; Tarantino et al., 2014) that are distinct from endosomal structures (Figures 2 and S2, see

also Movie S1). To further characterize the role of cytokine identity and dose on NEMO recruitment at CI-like puncta, we compared descriptive features such as their size and intensity across different cytokines and concentrations. Although properties of IL-1 and TNF-induced puncta did not show a clear trend across doses, IL-1-induced spots were significantly larger and brighter than their TNF-induced CI counterparts (Figure 2C and Movie S2; for all comparisons p-value $<< 10^{-10}$, student's t-test). To estimate the expected number of NEMO molecules in each complex, we evaluated intensity values for each fluorescent spot in terms of a reference live-cell reporter that recruits a known number of EGFP molecules into a diffraction-limited space (Wang et al., 2016). By comparing cells in identical imaging conditions, our analysis suggests that each of the larger IL-1-induced spots recruit approximately 300 NEMO molecules whereas TNF-induced spots recruit around 80 (Figures 2D & S2E).

Time-courses for NEMO complexes in single cells showed a peak in spot numbers between 10-20 minutes and a rapid falloff thereafter (Figure 2E), consistent with previous results from cytokine-induced IKK kinase assays (Werner et al., 2005; Werner et al., 2008). Numbers of NEMO spots per cell increased with cytokine concentration and showed a tendency of higher numbers in response to IL-1 at comparable molarities (Figure 2E & 2F). Taken together, these data indicate that the size and intensity of NEMO complexes depend on the type of engaged receptor, whereas the number of complexes is modulated by cytokine dose.

NF-κB responses are well-determined by descriptors of NEMO complexes.

Next, we investigated the relationship between cytokine-induced dynamics of NEMO and

RelA to ask whether NF-κB responses are well-determined by properties of fluorescent NEMO puncta when measured in the same cell. Time-courses for NEMO complexes and nuclear RelA localization were measured in response to a broad range of cytokine concentrations, and quantitative descriptors that summarize dynamic properties of EGFP-NEMO and mCh-RelA were extracted for each single cell (Figure 3A & 3B, see also (Lee et al., 2014; Zhang et al., 2017)). Scatterplots of descriptors showed that cytokines and concentrations together form a continuum with a strong monotonic relationship between descriptors of NEMO and RelA (Figure 3B and C). We also compared coefficients for determination between NEMO and RelA descriptors which showed stronger correlations when data are log-transformed (Figure S3). Increased R^2 values in log-space is because the NEMO-RelA relationship is likely governed by a power law, which is expected for a signal amplification mechanism with values that scale across orders of magnitude. Correlations between same-cell descriptors of NEMO and RelA revealed a strong effect size indicating that cell-to-cell variability in NF-κB response can be reasonably determined by descriptors of EGFP-NEMO (Figure 3C & 3D). Multiple linear regression for combinations of NEMO descriptors only marginally increased correlations (Figure S3C).

Previously, we showed that the 'Area Under the Curve' (AUC) and 'Maximum' (MAX) are scalar descriptors of a nuclear RelA fold-change time-course that encode the most information about cytokine dose (Zhang et al., 2017). Notably, among all descriptors for nuclear RelA fold-change dynamics, AUC_{RelA} and MAX_{RelA} also had the strongest correlation with same-cell descriptors of NEMO-recruiting complexes (Figure 3D; AUC_{NEMO} and MAX_{NEMO} respectively). Both NEMO descriptors also showed similar coefficients-of-determination for RelA descriptors, whether measured in terms of numbers

for EGFP-NEMO spots or aggregate intensity of EGFP-NEMO within complexes (Figure S3).

Overall, same-cell measurements of EGFP-NEMO and mCh-RelA reveal that the aggregate NF-κB response in a cell is well determined by the sum of NEMO recruitment to CI-like signaling complexes near the plasma membrane. Because enrichment of NEMO at ubiquitin-rich structures is an induced-proximity mechanism for kinase activation, it's reasonable that the AUC of EGFP-NEMO intensity in puncta is a strong proxy for downstream signaling. However, our characterization for the EGFP-NEMO fluorescence intensity at cytokine-induced spots showed wide-based distributions which could indicate that the amount of NEMO recruited at each spot varies significantly (Figure 2C). Nevertheless, the number of EGFP-NEMO puncta (MAX_{NEMO}) is almost interchangeable with AUC_{NEMO} as determinants of same-cell responses.

Cytokine environments control numbers and timing of NEMO complex formation. Asynchronous properties of EGFP-NEMO spots, such as when a spot forms or rates for NEMO recruitment and dissolution, will contribute to variability when spot intensities are measured from a snapshot image at a single time point. To understand the extent of inter-spot and between-cell variability, we used high-frequency imaging to enable tracking of each single spot over time (Figures 4, S4A, and Movie S3). Cells were stimulated with a step, pulse, or ramp in cytokine concentration in a microfluidic cell culture system (Mokashi et al., 2019) to observe how dynamic environments modulate properties of NEMO-recruiting complexes.

Tracking experiments revealed differences in fluorescence intensity time-courses,

where IL-1 induced EGFP-NEMO puncta were consistently brighter and longer-lived than TNF-induced puncta (Figure 4B). Both cytokines induce spots that peak within 2 to 3 minutes of detection followed by a decay phase where spots decline in intensity (Figure 4B and S4B). When stimulated with a cytokine pulse, most spots are detected only after the cytokine is removed (Figure 4C) demonstrating that formation of NEMO-recruiting complexes is variable and takes place up to 30 minutes following a stimulus. Step, pulse, and ramp stimulation further showed that the number of spots and the timing of spot formation are both modulated by the dynamics of cytokine presentation.

Descriptors for single spot trajectories showed remarkably low variability, in particular for the TNF response, when compared within the same cell or when the average of single-spot descriptors was compared between cells (Figure S4C and D). Analysis of the 'AUC spot intensity' descriptor (AUC_i) revealed a quadratic relationship between 'mean AUC_i' and 'AUC_i variance' for spots when measured in the same cell (Figure S4E). Increased variance between large NEMO-recruiting complexes may be due to steric properties of supramolecular assemblies. For example, where growth for certain types of ubiquitin polymers is spatially limited, or intact portions of large ubiquitin chains are clipped off en bloc or through endo-cleavage (Clague et al., 2019), leading to greater inter-spot variability. In nearly all cases, the coefficient of variation (CV) values for distributions of single-spot descriptors indicate that noise is lower than Poisson processes (Figure S4E). Together, our results suggest that dynamics of NEMO-recruiting protein complexes are strictly regulated for each cytokine response.

Negative feedback on NEMO complexes is primarily independent of transcription.

NF-κB-mediated expression of A20 and subsequent deubiquitinating (DUB) activity against NEMO-recruiting complexes constitute an essential negative feedback motif in inflammatory signaling (Nelson et al., 2004). Within tens of minutes, it's feasible that nascent A20 contributes to the decay phase of EGFP-NEMO spot numbers observed in whole-cell measurements (Figure 2E) thereby reducing IKK activation as observed in cell population assays (Werner et al., 2005; Werner et al., 2008). It was therefore unexpected that the decay phase for single EGFP-NEMO tracks is visible within several minutes of stimulation, which is remarkably fast for a feedback mechanism governed by transcription and translation (Figure 4B and S4).

To understand how different mechanisms of negative feedback impact trajectories of single EGFP-NEMO spots, we developed a model using ordinary differential equations. Here, cytokine stimulation induces formation of single spots at different times and each spot becomes larger and brighter with Michaelis-Menten kinetics to approximate ubiquitin polymer growth and EGFP-NEMO recruitment. The model considers two sources of negative feedback that act on NEMO-recruiting complexes by enhancing their disassembly rates. The first source aggregates the sum of NEMO-recruiting complexes to drive expression for an A20-like negative feedback mediator ('transcriptional feedback'; Figure 5A). The second source considers the impact from basal expression of A20 and other DUBs in resting cells before stimulation ('basal feedback'; Figure 5A). For both sources, the strength of negative feedback on each NEMO-recruiting spot increases with size to mimic DUB recruitment to ubiquitin polymers in the complex.

Using simulations to vary the strength for each source of negative feedback, their respective impacts on single-spot dynamics was apparent (Figures 5B and S5A). By

increasing the strength of basal feedback the decay phase for single-spot trajectories became steeper, and each spot displayed a sharp peak of intensity that was similar between spots regardless of when they form. By contrast, even though transcriptional feedback also increased steepness of the decay phase, the peak intensity of spots that form earlier were significantly greater than spots that formed later. For both sources, increasing strength of negative feedback reduces the overall peak height for all simulated spots (Figure S5A).

Based on simulations, if transcription is the predominant source of negative feedback, then spots that form later after cytokine stimulation are predicted to have lower maximum intensity, shorter track length, and smaller AUC (Figures 5B and S5). To test the prediction, we performed a reverse time-course experiment where imaging started after a delay relative to the time of cytokine stimulation (Figure 5C; 0, 5, 10, 15 minutes). Only new spots that formed within the first two minutes were tracked for each condition, thereby enabling direct comparison of early versus late-forming spots and minimizing effects of photobleaching. Biological replicates revealed that early- and late-forming single spot trajectories share highly similar dynamics (Figures 5B, 5C, and S5), suggesting that transcriptional feedback is dispensable in regulation of dynamics for CI-like complexes. We therefore repeated reverse time-course experiments in the presence of cycloheximide (CHX) to prevent translation of NF-κB-regulated genes, effectively breaking the transcriptional negative feedback loop. To verify that CHX inhibited protein translation, time-courses of nuclear NF-κB were also measured in the same cells during co-stimulation with IL-1 and CHX. NF-κB showed persistent nuclear localization in these cells indicating a disruption of the negative feedback loop mediated by IκBα protein

expression (Figure S5). Remarkably, loss of transcriptional feedback did not increase features of single spot trajectories as predicted by the transcriptional feedback model (Figures 5D and S5A). These results demonstrate that transcription is not the predominant mechanism of negative feedback on NEMO recruitment at CI-like complexes in the timescale of the primary cytokine response.

The IKK-NF-κB signaling axis has the architecture of a stochastic pooling network.

When TNF and IL-1 responses are considered separately, trajectories of EGFP-NEMO spots are highly similar regardless of when they form during a cytokine response. This observation argues that each complex behaves as an independent switch, that when activated recruits a quantized amount of NEMO over its lifespan. To understand information transmission properties of the IKK-NF-κB signaling axis, we abstracted the system into four phases (Figure. 6A). Detection ('i'), where parallel and independent CI-like switches provide redundant measurements of the same extracellular signal (S). Switching (ii) and amplification (iii), when a CI-like complex (CI) activates in response to S, it amplifies with a ligand-specific and quantized gain (G_L) of NEMO activity. The total cellular response (R) in terms of NEMO activity and subsequent NF-κB translocation is the summation (iv) of all amplifier gains in a cell, also referred to as 'signal pooling'. Although our live-cell data support independent binary switches, quantized amplification, and signal pooling of IKK into NF-κB (Figures 3, 4, and 5), conditions for detection (i) and switching (ii) remained ambiguous because of cell-to-cell heterogeneity.

The average number of NEMO spots within cells increases with cytokine concentration, yet, we see significant differences between single-cell responses in all

conditions (Figure 2F). To determine whether some cells are predisposed to stronger responses, or whether noise at the level of CI formation are predominant contributors to heterogeneity, we exposed cells to two sequential pulses of cytokines. Two-pulse experiments that compare the same cell in different conditions can be used to interpret the impact of stochastic noise on cell-to-cell heterogeneity (Adamson et al., 2016; Lipniacki et al., 2007; Sumit et al., 2019; Tay et al., 2010; Zhang et al., 2017). For these experiments, cells were first stimulated with a short low concentration reference pulse of cytokine followed by a nearly saturating concentration of cytokine to estimate the maximum number of CI complexes (CI_{max}) that each cell can produce (Figure 6B). In cells exposed to the same cytokine for both stimuli, the rank ordering of single cell responses to the reference stimulus is strongly correlated with CI_{max} for the same cell (Figure 6C; Spearman $\rho > 0.70$, p-value $< 10^{-10}$). We then asked whether the correlation was due to shared mechanisms downstream of TNF and IL-1 receptors in cross-pulse experiments where cells are exposed sequentially to both cytokines. Same-cell correlations in cross-pulse experiments were greatly reduced with marginal to non-significant p-values (Figure S6). These data suggest that cells are predisposed to different responses based on cell-to-cell variability in receptor-specific components of CI-complexes.

Taken together, our data are consistent with the architecture presented in Figure 6A. Here, the number of CI_{max} is receptor-specific and varies between single cells, and the cell's response to a sub-saturating 'S' is fractional to its CI_{max}. Together with same-cell NEMO and RelA data, our results support a generalization of cytokine-IKK-NF-κB signaling that is evocative of a stochastic pooling network (SPN), a model sensory system with noise-mitigating and information-compressing properties (McDonnell, 2009). An

important difference however, is that while binary detectors in an SPN transmit on-off measurements about an information source, each NEMO-recruiting complex performs amplification with a gain determined by the cytokine-receptor-complex identity. Henceforth, we refer to the network architecture as a variable gain SPN (VG-SPN).

Stochastic pooling mitigates noise and fine-tunes response magnitude at the expense of information.

Identification of the VG-SPN architecture enabled us to conceptually characterize signal transduction properties that could not be measured from single-cell IKK data due to limited experimental throughput. We first considered the impact of the number of CI switches and their associated gains on noise propagation in the resulting VG-SPN. A mathematically-controlled comparison (Alon, 2007; Savageau, 1976) between different network configurations was enabled by assuming each configuration is capable of producing the same maximal steady-state response (R_{max}; Figure 7A). Simulations for different mathematically-controlled configurations of the VG-SPN demonstrated that shot noise associated with signal detection, and noise associated with the signal gain, both fall off rapidly with increasing numbers of CI switches (Figure 7B). Noise from these sources can be mitigated almost completely when cells are capable of forming ~100's-1000's of CI per cell (CI_{max}/cell). Here, noise-mitigation benefits can be attributed to signal parallelization through quantized nodes. For example, gain noise at each CI can be positive or negative, and because each CI is independent, the distribution for noise across all CI in a cell is centered near zero. Summation of signaling through R_{max} in a VG-SPN effectively averages the contribution of noise across all CI/cell, which is ideally zero

assuming sufficient parallelization and absence of other biases. See also Methods for similar description of shot noise mitigation.

Next, we explored the information transmission properties for different VG-SPN configurations by calculating their channel capacities (Selimkhanov et al., 2014). We assessed the VG-SPN model using parameters obtained from our single-cell IKK data and simplifying assumptions about distributions for CI properties (see methods for details, and hyperparameter tuning in Figure S7). For these simulations, CI_{max}/cell and amplifier gain G_L were allowed to vary independently. Consistent with our previous analysis for noise-propagation in VG-SPNs, when G_L is greater than 10 molecules per complex the channel capacity increases with the number of CI_{max}/cell and rapidly approaches saturation (Figure 7C, bottom). The maximum channel capacity was found to be 2.5 bits with the model calibrated to live cell data (Figure S7), suggesting a theoretical maximum for information transmission at the level of CI. However, for G_L values of 10 or lower, the system requires orders-of-magnitude more CI_{max}/cell to reach comparable channel capacity values. We also calculated the maximum response (R_{max}) which shows an inverse linear relationship, where different configurations of CI_{max}/cell and G_L can achieve activation of the same number of response molecules up to arbitrarily high numbers (Figure 7C, top). Taken together, the VG-SPN motif generates trade-offs, and although the motif results in hard limits for the information content of a signaling pathway, it is also parsimonious and robust to stochastic noise and cell-to-cell variability in protein abundances.

Discussion:

Endogenously expressed EGFP-NEMO is a multifaceted reporter that reveals several aspects of signal transmission. At the level of detection, there is agreement between numbers of EGFP-NEMO puncta induced by saturating cytokine concentrations and average surface receptor numbers in U2OS cells (Figures 1 and 2). Similarly, the timing of formation of EGFP-NEMO puncta establishes when ligand-receptor-adapter assemblies become capable of signaling in the cytoplasm. Continuous stimulation experiments show that most EGFP-NEMO spots form within 5-10 minutes, indicating that cytoplasmic components of CI-like complexes are not limiting. However, in cells exposed to a short pulse, new spots form up to 30 minutes following cytokine removal, demonstrating variability in timing for receptors to assemble into a signaling-competent stoichiometry. In the cytoplasm, spot intensity time-courses inform about biochemical interactions and feedbacks linked to signal amplification. Here, families of different ubiquitin ligases, kinases, and DUBs engaged at CI-like structures establish rates of EGFP-NEMO recruitment and dissolution. Distinct properties between puncta initiated by different receptor superfamilies (Figures 2-5) suggest that various adapters and ubiquitin requirements associated with different types of CI-like complexes will determine cytokine-specific signal amplification (Clague et al., 2019; Ikeda et al., 2011; Komander and Rape, 2012; Tarantino et al., 2014; Wertz et al., 2004). We therefore expect endogenous EGFP-NEMO will be valuable in unraveling these upstream mechanisms of inflammatory signaling, similar to reporters for NF-κB that have contributed richly for well over a decade.

Notably, imaging requirements for EGFP-NEMO limit experimental throughput, in particular for spot tracking experiments that require both high magnification and high

frequency time-lapse. Although dynamical properties of NF-κB signaling are important mediators of information transmission, analyses that calculate information metrics require a large number of single-cell data points (Cheong et al., 2011; Selimkhanov et al., 2014; Zhang et al., 2017). Consequently, our analysis of EGFP-NEMO required simplifications through coarse-grained scalar descriptors that summarize dynamic properties of NEMO-recruiting complexes and nuclear RelA localization in the same single cells. Our analysis revealed two descriptors of EGFP-NEMO that are strong determinants for descriptors of RelA that were previously shown to carry the most information about cytokine concentrations in the milieu (Zhang et al., 2017). As technologies emerge that enable data collection for calculation of information metrics between both reporters in the same cell, determination is likely to improve. However, it is also rational that the aggregate sum of NEMO in CI-like complexes during a primary cytokine response is a strong same-cell determinant of the accumulated NF-κB response. This deterministic relationship may therefore remain among the strongest in coming years, providing a read-out for signaling flux and disease-associated perturbations at the level of CI.

Induction of A20 transcription is considered a defining negative feedback in the NF-κB response (Ashall et al., 2009; Werner et al., 2005; Wertz et al., 2004). However, tracking experiments revealed that trajectories of early and late-forming EGFP-NEMO spots are remarkably similar and insensitive to CHX (Figure 5). Although this does not preclude non-catalytic roles for A20 in regulation of IKK (Skaug et al., 2011), it demonstrates that each CI-like complex is independent and not influenced by transcriptional feedbacks from complexes that form earlier during a response in the same cell. Our data therefore support another proposed role, where transcriptional feedback

via A20 is not primarily directed at the initial immune response but instead establishes a new baseline for tolerance to subsequent stimuli (Werner et al., 2008). Taken together, signal amplification and negative feedback at each CI-like complex is determined predominantly by the resting cell state.

Abstraction of our experimental observations revealed a VG-SPN signaling architecture (Figures 5 and 6). The resulting model enabled us to investigate *in silico* the emergent properties of IKK-NF-κB at the level of cytokine detection and signal amplification. With detection and parallel signal amplification at independent CI nodes, our model revealed that noise is effectively mitigated with 100's - 1000's of signaling complexes, and greater numbers have diminishing returns per complex for information transmission. Further benefits to signal transmission through a CI amplifier allow cells to fine tune numbers of activated cytoplasmic signaling molecules, which are significantly more abundant than cytokine receptors at the cell surface. For NF-κB signaling, high-gain amplification enables a large repertoire of receptors to engage the same cytoplasmic pool of IKK with limited occupancy of space at the cell surface. Cells can therefore favor parsimony in receptor numbers, or increase receptor numbers with reduced amplification gain, to interface with the same size pool of signaling molecules while preserving information transmission. These trade-offs provide orthogonal controls to robustly fine tune or diversify response sensitivity to stimuli, as shown here for different cytokines.

The classic model of chemoreception (Berg and Purcell, 1977), established limitations for the signal-to-noise relationships in biological sensing systems that use time-averaged receptor occupancy to measure chemical concentration. By contrast, multivalent cytokines exhibit markedly increased apparent affinity over bimolecular

interactions and therefore limit the likelihood of ligand dissociation from mature signaling complexes. Although these signaling systems are distinct, they are both reducible to the same motif with alternative definitions for amplification gain, and possibly with different pooling functions. A remaining question is why biological sensory systems would converge on SPN-like architectures? Although several conceptual benefits and limitations of VG-SPNs are discussed here, other general properties of SPNs may also contribute to the answer. Stochastic resonance is an example of a counterintuitive property of SPNs that uses stochastic fluctuations to enhance information transmission (McDonnell, 2009; McDonnell and Abbott, 2009). Although the number and timing of CI-like switches is stochastic and subject to noise during cytokine responses, they can theoretically enhance information transmission over an array of noiseless binary switches. An array of perfect switches that simultaneously activate at the same signal threshold is a binary system, either all ‘on’ or all ‘off’, whereas stochasticity in the fraction and timing of CI formation increases the number of system states through probabilistic interactions with the milieu.

In summary, our live-cell experiments revealed CI-like complexes are independent and switch-like, where each complex recruits a quantized amount of IKK over its lifespan. These were unexpected results that led to conceptual simplification and identification of the underlying signaling architecture. However, independence between detector nodes is not a required characteristic of a VG-SPN and most receptor signaling systems can therefore be viewed through a similar lens. We expect the VG-SPN is common to receptor-signaling systems, each with distinct pooling functions, feedbacks, and feedforwards that will reveal their individual trade-offs and information transmission benefits to the cell.

Acknowledgements:

We thank Steven Smeal, James Faeder, Anne-Ruxandra Carvunis, Nathan Lord, and Suzanne Gaudet for helpful discussions. JAC would like to dedicate this work to the memory of his mother: Norma Graciela Vasquez Vargas. **Funding:** This work was supported in part to JAC from The American Association of Immunologists Intersect Fellowship Program for Computational Scientists and Immunologists, in addition to generous funding to RECL from NIH grant R35-GM119462 and the Alfred P. Sloan Foundation.

Author contributions:

Conceptualization: JAC, CSM, RECL. Methodology: JAC, CSM, GJK, YG, SAG, DLS, QZ, RECL. Software: CSM, GJK, SAG. Formal analysis: JAC, CSM, GJK, YG, DLS. Investigation: JAC, CSM, YG, CSM, QZ. Writing – original draft: JAC, CSM, RECL. Writing – review and editing: JAC, CSM GJK, YG, SAG, DLS, QZ, RECL. Visualization: JAC, CSM, RECL. Supervision and funding acquisition: RECL.

Declaration of Interests:

The authors declare no competing interests.

Figure Titles and Legends:

Figure 1: Differential expression of cytokine receptors enables cells to selectively respond to their environment

(A) Schematic of cognate receptors for TNF and IL-1 cytokines. Monomeric receptors and receptors that engage with decoy receptors (IL-1R2) are inactive and do not transmit signals into the cytoplasm (left). Activated receptor complexes (right), consisting of a TNFR homotrimer bound to TNF or an IL-1R1-IL-1R3 heterodimer bound to IL-1, are capable of seeding CI-like complexes in the cytoplasm. **(B)** Quantification of surface receptor expression on single U2OS cells. The average of 3-7 biological replicates is shown for each condition. Error bars represent SEM. See also, Figure S1.

Figure 2: Size and intensity of NEMO complexes are modulated by cytokine identity independent of dose

(A) Maximum intensity projections from 3D time-lapse images of endogenous EGFP-NEMO show rapid recruitment to CI-like complexes in cells exposed to IL-1 or TNF. See also Movies S1 and S2. **(B)** Detail of fluorescent complexes (orange and blue boxes in panel A) show differences between responses to IL-1 and TNF. Scale bar represent 20µm for all. **(C)** Histograms summarizing the size (left) or intensity (right) of EGFP-NEMO complexes across concentrations of IL-1 (orange) or TNF (blue). Distributions represent single-cell data in aggregate from 3-5 experiments. Vertical bar indicates the median of each population. Comparison between all conditions, IL-1-induced complexes are larger and brighter than TNF-induced complexes (p-value $<< 10^{-20}$; t test). Numbers of cells analyzed and associated spot numbers are provided in Table S1. **(D)** Boxplot for estimates of the total number of EGFP-NEMO molecules in each CI-like complex. Median

and interquartile ranges are indicated. See also methods and Figure S2E. **(E)** Single-cell time-courses for the number of EGFP-NEMO complexes in cells exposed to concentrations of IL-1 (orange) and TNF (blue) as indicated. **(F)** Dose response of maximum number of EGFP-NEMO complexes. Dark orange and blue lines represents the median and vertical bars represent the interquartile range for cells stimulated with IL-1 or TNF respectively. See also, Figure S2.

Figure 3: Same-cell NF-KB responses are determined by number and intensity of NEMO complexes

(A) Maximum intensity projections from 3D time-lapse images of EGFP-NEMO (top) and mCherry-RelA (bottom) expressed endogenously in the same U2OS cells. Cells were stimulated with 10 ng/mL IL-1. **(B)** Diagrams indicating time-course descriptors for EGFP-NEMO complexes (top) and nuclear fold-change of mCherry-RelA (bottom) in single cells. RelA features are similar to those used previously (Lee et al., 2014; Zhang et al., 2017). **(C)** Example of a strong same-cell correlation between single-cell descriptors of EGFP-NEMO complexes and nuclear RelA fold change. IL-1 and TNF responses across all doses overlap and form a continuum that relates the paired descriptors. **(D)** Heat map of spearman rank ρ-values for all pairs of same-cell descriptors for IL-1 (left) and TNF responses (right). See also Figure S3 and Table S2 for summary of cells per condition.

Figure 4: The number and time of NEMO complex formation is determined by the extracellular environment

(A) Maximum intensity projections from high frequency 3D time-lapse imaging experiment

of cells exposed to 100 ng/mL IL-1. Colored lines in overlay indicate tracks for individual EGFP-NEMO complexes over time. On average, 60-75% of detected complexes are associated with a track of significant length (Figure S4A). Scale bar represent 20µm, see also Movie S3. **(B)** Time-courses of fluorescence intensity for single tracked EGFP-NEMO complexes in cells stimulated with indicated conditions in a microfluidic cell culture system (Mokashi et al., 2019). Two representative single-complex trajectories are F(1) average number and the time of formation for tracked EGFP-NEMO complexes. On average, 10 cells were analyzed in each condition. Error bars represent the SEM. See also, Figure S4.

Figure 5: The primary NEMO response is independent of the transcriptional feedback loop

(A) Schematic of the hybrid deterministic−stochastic (HyDeS) model of basal (red arrows) and transcription-dependent (blue arrows) feedback regulation of NEMO complexes. Each growing CI-like complex will recede with rates that depend on recruitment of deubiquitinating enzymes (DUB). **(B)** Simulations of individual EGFP-complex trajectories using the model in Figure 5A, considering: no feedback (top left), transcription-dependent feedback only (top right), basal feedback only (bottom left), or combined transcriptional and basal feedback (bottom right). **(C)** Schematic of reverse time-course experiments. Only new EGFP-NEMO complexes that form within the first 2 minutes are tracked in movies from each high-frequency imaging experiment. Cells were stimulated with 100 ng/mL concentrations of either IL-1 (top) or TNF (bottom). **(D)** Boxplots of maximum intensity of individual EGFP-NEMO complexes trajectories after stimulation with IL-1 (top)

or TNF (bottom) in cells pretreated for 20 minutes with media plus DMSO (left) or cycloheximide (CHX, right). Co-stimulation with CHX does not significantly increase values for single spot descriptors as predicted by the transcriptional feedback model (see also Figure S5). Median and interquartile ranges are indicated, and biological replicates are shown side-by-side with increased transparency for each experiment. See also, Figure S5.

Figure 6: Switch activation in the VG-SPN is governed by cell-intrinsic properties

(A) The VG-SPN consists of 4 phases, detection, switching, amplification, and signal pooling. For detection, each CI-like complex (CI) is modeled as one of 'j' independent switches with an activation probability proportionate to the signal strength. During switching and amplification, each activated switch amplifies the signal with gain 'G_L', related to the number of NEMO molecules recruited by each CI-like complex. Subsequently, NEMO from each CI-like complex is added to the cytoplasmic 'pool' of activated signaling molecules. **(B)** Schematic for a 2-pulse experiment. Cells are first exposed to a short and low concentration reference pulse of cytokine. Subsequently the same cells are exposed to a second pulse of cytokine at saturating concentrations intended to reveal the maximum number of CI complexes that can be generated by each cell (CI_{max}). **(C)** Single cells are rank-ordered by their response to reference cytokine stimulation and correlated with their CI_{max} values. Responses to TNF (top) and IL-1 (bottom) are shown. Inset numbers indicate Spearman's rank correlation (ρ) and associated p-values. See also, Figure S6.

Figure 7: VG-SPNs generate trade-offs between noise mitigation, response magnitude, and information transmission

(A) Different configurations of the VG-SPN. For a mathematically controlled comparison, CI and 'G_L' are adjusted so that each configuration can achieve the same maximum response (R_{max}). **(B)** Detection introduces shot noise (top), where a switch activates erroneously with a probability given by the shot noise level. Since each CI is independent, shot noise is mitigated through parallelization via multiple CI until a 'noise floor' is achieved. The noise floor is determined by the shot noise value. Variability in the gain from each CI switch (bottom) introduces noise during transmission. Gain noise is effectively averaged and approaches zero via parallelization of independent switches. **(C)** Maximum response (R_{max}; upper limit was set to 10^7 response molecules per cell) and relative channel capacity corresponding to different VG-SPN configurations (see also Figure S7). The VG-SPN architecture provides ligand-specific tunability and robustness to noise.

Methods:

Cell Culture

Parental KYM1 (female), HeLa (female), and U2OS (female) cell lines were obtained from ATCC, and HeLa cell line stably expressing scFv-GFP and tdPCP-tdTomato were a kind gift from Dr. Xiaowei Zhuang from Harvard University (Wang et al., 2016). All cell lines were cultured in RPMI (KYM1), DMEM (HeLa), or McCoy's 5A (U2OS) media at 37°C and 5% CO2. All media were supplemented with 10% Corning Regular FBS, 100 U/mL penicillin, 100 µg/mL streptomycin and 0.2mM L-glutamine (Invitrogen). Cells were periodically monitored for mycoplasma contamination.

Quantitative Flow Cytometry

Fluorescence-activated cell sorting (FACS) analysis of samples and PE-beads were performed in a BD LSRFortessa machine (University of Pittsburgh-Department of Immunology Flow cytometry facility). We used Phycoerythrin (PE)-conjugated beads (BD Biosciences, Cat. # 340495) and PE-conjugated antibodies against the following human proteins were obtained from R&D systems: TNFR1 (FAB225P), TNFR2 (FAB226P), IL1R1 (FAB269P), IL1R2 (FAB663P), IL1R3 (FAB676P), polyclonal goat IgG PE-conjugated (IC108P) and mouse IgG1 PE-conjugated (IC002P). Cells were maintained and used between 5-15 passages. For de-attaching cells from plates, we use 2 mM EDTA in cold PBS. Forty-eight hours before staining 1-2x10^5 cells were plated in 6-well plates. On the day of the staining cells were de-attached from the plate, transferred to polypropylene microtiter tubes (2681377, Fisherbrand™), and maintained on ice during the entire process. Fc-receptors were blocked using human BD Fc block antibody

(564219) for 10-15 minutes in the dark. Next, cells were washed with 2% FBS in PBS (FACS buffer) and incubated with primary antibodies for 1 hour at 4°C in the dark. Next, samples were washed twice, and resuspended in 1 ug/mL DAPI (Cat#: D1306, Invitrogen) in FACS buffer between 0.5-1.5 hours before data acquisition. Data analysis was performed using FlowJo™ (BD, version 10.6.1_CL). Samples stained with PE isotype controls were used to set the background fluorescence by subtracting their mean fluorescence intensity (MFI) to the MFI of samples stained with specific antibodies. Next, we used the MFI from PE-conjugated beads to estimate the number of PE molecules on the surface of each cell. All these antibodies have been previously used to estimate surface receptors, with accepted 1:1 ratios of PE to antibody molecules (Bebes et al., 2014; Bryl et al., 2005; Serke et al., 1998).

Fixed-cell Immunofluorescence

U2OS WT and U2OS cells stably overexpressing NEMO cells were seeded into plastic flat bottom 96-well imaging plates 24 hours before cytokine treatment at a density of 7000 cells/well. On the day of the experiment, wells receiving IL-1 or TNF (10 ng/mL or 100 ng/mL, respectively) were stimulated 45 min prior to fixation. Pre-warmed 15X cytokine mixture was spiked into wells and mixed. After treatment and before fixation the cells remained in environmentally controlled conditions (37°C and 5% CO2). Cells were fixed with 4% PFA and permeabilized using 100% methanol for 10 minutes each with one PBS wash in between, and three PBS-T (PBS 0.1% Tween 20) washes at the end. Next, cells were incubated in primary antibody solution (3% BSA in PBS-T) with 1 µg/mL of both α-RELA (sc-8008; Santa Cruz) and NEMO (sc-8330; Santa Cruz) at 4°C overnight. The

following morning, cells were washed three times with PBS-T and incubated for 1 hour at room temperature with secondary antibody solution in 3% BSA in PBS-T (4 µg/mL of both goat anti-Mouse IgG Alexa Fluor 647 (A21235; Thermo) and goat anti-Rabbit IgG Alexa Fluor 594 (A11012; Thermo). After incubation, cells were washed twice in PBS-T and incubated in 200ng/mL Hoechst in PBS-T for 20 min. Finally, wells were washed in PBS-T and left in PBS to keep cells hydrated during imaging. Cells were imaged using Delta Vision Elite imaging system at 20x magnification with a LUCPLFLN objective (0.45NA; Olympus).

Fixed Cell Image Analysis

Using Cell profiler (www.cellprofiler.org, (Lamprecht et al., 2007)), cell nuclei were segmented using the Hoechst channel labeling DNA. Next, secondary segmentation was performed using EGFP-NEMO channel to define the cellular boundaries. The output of cell segmentation was compiled and analyzed using custom scripts in MATLAB (Mathworks, R2019b).

Establishing EGFP-NEMO/mCherry-RELA CRISPR Double Knock-in Cells

Single knock-in U2OS cell lines expressing EGFP-RELA/NEMO were generated previously using CRISPR-Cas9 technology as described in reference (Pabon et al., 2019). To generate double Knock-in cells, we assembled the RELA repair template consisting of DNA sequences for a left homology arm (LHA −544 bp, chromosome 11_65663376–chromosome 11_65662383) followed by a mCherry protein coding sequence with a start codon but no stop codon and a sequence encoding 3x GGSG linker

in-frame with the right homology arm (RHA +557 bp, chromosome 11_65662829–chromosome 11_65662276) from plasmids synthesized by GeneArt. Synonymous mutations were introduced to prevent interaction of the repair template and Cas9. Next, single EGFP-NEMO Knock-in U2OS cells were seeded in 6-well plates (2 x 10^5 cells) and transfected next day with pSpCas9n-(BB)-2A-Puro-RELA_gRNAs and Bgl2-linearized mCherry-RelA repair template donor plasmid. A ratio of 3.5:1 FuGENE HD (Promega) to total DNA was used for transfection of 4 µg of DNA. Plasmids generation, and CRISPR modifications were all based on Ran et al. 2013 (Ran et al., 2013).

Live-cell Imaging

Live cells were imaged in an environmentally controlled chamber (37 °C, 5% CO2) on a DeltaVision Elite microscope equipped with a pco.edge sCMOS camera and an Insight solid-state illumination module (GE). For detection of NEMO spots, U2OS cells expressing fluorescent protein (FP) fusions of RELA and NEMO were seeded at a density of 15,000 cells/well 24 h prior to live-cell imaging experiments on no. 1.5 glass bottom 96-well imaging plates (Matriplate). Medium was changed to phenol red-free FluoBrite Dulbecco's modified Eagle's medium (Gibco, A18967–01) between 30 min to 2 h before imaging. For detection of NEMO spots, live cells were stimulated with the indicated concentrations of TNF or IL-1. After cells adapted in the environmentally controlled chamber, we collected eight z-stack images of 0.5 µm separation in the Alexa Fluor 488 channel with an exposure of 0.04 sec and a transmission of 32%. Using these stacks of images, we reconstructed NEMO spots in 3D using image J (for display) and dNEMO (more details in "Punctate Structures Detection and Quantification" section). To test our

different hypothesis, we performed two types of time-lapse imaging experiments: long-term and short-term high-frequency imaging. Images were collected over at least 3 fields per condition with a temporal resolution of 2 min per frame for long-term and 10 seconds per frame for short-term high-frequency imaging experiments. Wide-field epifluorescence and DIC images were collected using a ×60 LUCPLFLN objective. For all treatments, cytokine mixtures were prepared and prewarmed so that addition of 120 µL added to wells results in the indicated final concentration.

For 2-pulse experiments, cells were exposed to a 1-minute dilute 'reference pulse' of either TNF or IL-1, selected from calibration experiments to produce a subtle response in most cells (2 and 5 ng/ml for TNF and IL-1 respectively), followed by a 'saturating pulse' of 500 ng/mL for same-cell comparisons. Cells were washed once with pre-warmed fresh media during media swaps. Since EGFP-NEMO foci form and disperse rapidly after treatment, a 30 minute recovery period was selected between 'reference' and 'saturating' pulses. The short recovery period also minimized the effects of photobleaching which were apparent within 60-90 minutes of imaging.

For small molecule inhibitors experiments to study the nature of the NEMO spots, we pretreated cells with 178 µM CHX, 50 µM MDC, or 20 µM Dynasore for 20 minutes before adding cytokine on top of the medium with inhibitor.

Live Cell Imaging in Microfluidic Devices

Microfluidic device fabrication and operation was done as described previously (Mokashi et al., 2019). Briefly, dynamic stimulation devices of two inlets and one outlet were made with PDMS (Sylgard), autoclaved, washed with ethanol, and incubated with a solution of

0.002 v/v fibronectin in PBS for 24 hours at 37 °C. After incubation, excess of fibronectin was flushed with tissue culture media multiple times. Between $3x10^6$ and $8x10^6$ cells/ml were seeded by inserting 200 µl pipette tip in the outlet port. The outlet port was plugged with PDMS plugs after reaching a cell density for approximately 60% confluence. The device was incubated for at least 24 hours and PDMS plugs at the outlet were then replaced with pipette tips filled with medium. On the day of the experiment, tygon tubes (Fisher Scientific 1471139) were attached to the device with the other end connected to basins with media or cytokine treatment. The basins were then placed on corresponding platforms on the gravity pump and the attached tygon tubes were clamped. The device was then fitted to a custom adapter and placed under the microscope for imaging. The clamps on the tubes were removed at the beginning of the experiment. Cells were stimulated with desired pattern of cytokine stimulation (pulse, ramp or continuous) by changing the heights of basins by controlling corresponding stepper motors through custom codes uploaded on the Arduino mega 2560 microcontroller. The cytokine treatment was prepared with Alexa647-conjugated BSA (0.0025 v/v; Invitrogen) and imaged with CY5 filter to confirm the corresponding stimulus pattern. Images were collected under same conditions as previously described for live-cell imaging.

Punctate Structures Detection and Quantification

EGFP-NEMO and SunTag polysome spots were detected and quantified using our application dNEMO (Kowalczyk et al., 2020). Briefly, dNEMO is a computational tool optimized for measurement of fluorescent puncta in fixed-cell and live-cell time-lapse images. The user-defined threshold for spot detection in dNEMO was set between 1.5

and 2.0 for all images. Reported pixel values for puncta were individually background-corrected by averaging pixels from an annular ring surrounding each spot. The width and offset for the annular ring were both set to 1 pixel. We furthermore stipulated that puncta must appear in at least 2 contiguous slices of the 3D images (out of 8 slices) to be considered valid. The same user parameters were applied to all images and single cells were manually segmented using dNEMO's keyframing function. For each single cell, spot features were measured for each new spot that formed following stimulation, yielding sets of single-cell spot features over time. NEMO puncta flat-field and background-corrected images were prepared for display using ImageJ.

Tracking of Individual NEMO Spots

The location and intensity data of EGFP-NEMO spots obtained with our dNEMO software (Kowalczyk et al., 2020) was used for single-spot tracking using the uTrack package in MATLAB (Jaqaman et al., 2008). The hyperparametrs in the uTrack package were adjusted to enhance tracking performance for TNF and IL-1 induced spots. Specifically, the time gap window was lowered to 3 frames and the gap penalty was lowered to 1 from their default values of 5 and 1.5 respectively. The minimum length of tracks segments used for gap closing was increased to 3 frames from the default of 1 frame. The merging and splitting events were considered while tracking. Properties of individual spots (intensity, size etc.) were then associated with tracking data to generate single-spot trajectories for each spot property. Trajectories lasting for less than 3 minutes were excluded from further analyses. With these settings, approximately 60% and 75% of spots respectively for TNF and IL-1 responses were tracked and included in subsequent

analysis (Figure S4A). Three main features were obtained from each single-spot trajectory:

1. Maximum intensity or Max_i (peak intensity of a single-spot trajectory)
2. Integrated intensity or AUC_i (sum of spot intensities at all time-points in a trajectory)
3. Track length (trajectory length i.e. time for which the spot is tracked)

Features of single-spot trajectories were then compared for dynamic stimuli experiments involving different cytokines across different cells (Figure S4); and for spots formed at different time-windows in reverse time course experiments (Figures 5D and S5).

Estimating Number of NEMO Molecules per NEMO Spot via Calibration with SunTag Labeled Polysomes

To quantify the number of NEMO molecules within each NEMO complex (spot), the CRISPR labeling of NEMO with EGFP allows us to infer the number of NEMO molecules by counting GFP molecules and converting with 1:1 ratio. In counting GFP molecules in NEMO puncta, we utilized the live cell translation reporter developed by Chong Wang et. al, (Wang et al., 2016) to calibrate the relation between GFP counts and measured GFP intensity and imaged it in HeLa cells with the same imaging condition used for NEMO in U2OS EGFP-NEMO cells.

During translation, one mRNA binds to multiple ribosomes simultaneously and form a large polysome complex. We assume that the positioning of each ribosome on mRNA independently satisfies a uniform distribution. The signal intensity of each fluorescence foci in the cytoplasm, representing the translating polysomes, varied depending upon the total number of ribosomes and the location of each ribosome on

mRNA. When ribosomes reach the region after the coding sequence for the SunTag peptide, the intensity would be the maximum for fully assembled complex; when ribosomes are halfway towards the end, the signal would be approximately half maximal. To account for this variability, we used Monte Carlo simulations to randomly sample the positions of ribosomes and generate the distribution of numbers of SunTag peptides being produced when there are n ribosomes present on single mRNA, denoted by p_2 (m,n), where m is the number of SunTag. n, as the number of total ribosomes on each mRNA, satisfies Poisson distribution p_1 (n)=e^(-λ) λ^n/n!. The average number of ribosomes for each translation foci is measured to be 12 experimentally (Wang et al., 2016), therefore we set λ ≈ 12. The possibility of m SunTag peptides being translated on each translation foci are calculated as follows:

$$P(m) = \sum_{n=1}^{+\infty} p_2(m,n)p_1(n)$$

When n is large, p_1 (n) rapidly converges to zero. Therefore, we set n = 30 as the cutoff of the summation.

We quantified the fluorescence intensity of individual translating polysome in HeLa cells using dNEMO (Kowalczyk et al., 2020) with the same threshold used for NEMO quantification in U2OS cells. As the GFP intensity is proportional to the number of GFP molecules, we determined the scaling factor between the measured fluorescence intensity and theoretical distribution of GFP molecule numbers. Here, we used the Nelder-Mead algorithm to minimize the square of difference between the “measured” GFP distribution and theoretical GFP distribution to obtain the scaling factor. To account for effects of photobleaching, we calculated the scaling factors independently for each frame

of the time-lapse image. Using the scaling factor obtained from the translation reporter, the intensity of NEMO spots was converted to numbers of GFP molecules per spot.

Extracting Descriptors from NF-κB Dynamics

Descriptors of the fold-change of the FP-RELA mean intensity trajectories were extracted using custom MATLAB scripts and Image J movie explorer. The fold-change transform is carried out by dividing the FP-RELA trajectories by the initial nuclear fluorescence at the zero-time point. Those descriptors include:

- Area under the fold-change curve (AUC_{Fold}): a summary statistic which approximates the cell's response over time, previously found to carry the most information about a cell's response to cytokine stimulation (Zhang et al., 2017).
- Max fold change (F_{max} / $F_{initial}$): maximum value of the fold-change trajectory, previously found to determine the transcriptional response of cells stimulated with TNF (Lee et al., 2014).
- Maximal rate of nuclear entry ($Rate_{in}$): slope of line fitted to three data points between time zero and time of maximum fold change. Point along fold-change trajectory at which slope was determined was point where slope had maximal absolute value.
- Maximal rate of nuclear exit ($Rate_{out}$): slope of line fitted to three data points between time of maximum fold change and the end of the fold-change trajectory. Point along fold-change trajectory at which slope was determined was point where slope had maximal absolute value.
- Time of max ($t_{max\ (fold)}$): time at which fold-change is maximum.
- Time of half up ($t_{50up\ (fold)}$): time point at which fold-change trajectory rises to half the

max fold change.

- Time of half down ($t_{50down\ (fold)}$): time point at which fold-change trajectory falls to half the max fold change.

Extracting Descriptors from EGFP-NEMO Dynamics

Descriptors of trajectories for the NEMO spot number and NEMO spot intensity were extracted from single cell and single complex data using custom MATLAB scripts. The NEMO spot number trajectory is the number of NEMO spots detected per cell over time, while the NEMO spot intensity trajectory is the integrated intensity of the detected spots per cell over time. Those descriptors (per trajectory) include:

- Area under the curve (AUC): area under the trajectory integrated. For a given cell's NEMO spot number and spot intensity trajectories, this represents either the total number of spots detected, or the total intensity of the spots detected, respectively.
- Maximum value (Max): maximum number of spots / spot intensity for a given cell trajectory.
- Rate of entry ($Rate_{in}$): slope of line fitted to three data points between time zero and time of max. Point along trajectory at which slope was determined was point where slope had maximal absolute value.
- Rate of exit ($Rate_{out}$): slope of line fitted to three data points between time of max and the end of the trajectory. Point along trajectory at which slope was determined was point where slope had maximal absolute value.
- Time of max (t_{max}): time at which the NEMO spot trajectory trajectory is maximal.
- Time of half up (t_{50up}): time at which the NEMO spot trajectory rises to half the

maximum value.

- Time of half down (t_{50down}): time at which the NEMO spot trajectory falls to half the maximum value
- Full width at half max (FWHM): width of the peak of the NEMO spot trajectory between the time of half up and the time of half down.
- Maximum over area of the cell (Max/Area): maximum value of the NEMO spot trajectory divided by the area of the cell. The cell's area is given by the polygon output from the dNEMO results.
- Fold-change peak difference ($t_{max\ (fold)}$ - t_{max}): difference between the time of maximum fold change and the time of max of the NEMO spot trajectory.

Correlation and Multiple Linear Regression of NEMO and NF-κB Descriptors

Descriptors collected from both the FP-RELA and EGFP-NEMO trajectories were correlated using Spearman's rank and coefficient of determination in linear and log-log scales (see Supplemental Figure S3). When correlation between a pair of descriptors could not be computed (e.g., an inability to compute some trajectory's $rate_{in}$ or t_{max} in cells that did not respond significantly to stimulation), the single cell was omitted from the affected correlation dataset, but not from the overall set of cell trajectories being analyzed. Multiple linear regression was also applied to the linear and log-transformed descriptors of the cells responding to TNF, IL-1, or the full combined experimental dataset (see Supplemental Figure S3). Linear correlation and multiple linear correlation of the descriptor sets was carried out using custom MATLAB scripts**.**

Computational Model (HyDeS) to examine relative effects of Basal and Transcriptional feedback on NEMO spot dynamics

We modeled the intensity of individual NEMO spots with a hybrid deterministic-stochastic (HyDeS) model. The purpose of this model is to examine the relative effects of basal and transcriptional feedback via DUB molecules on NEMO spot dynamics, and not necessarily to capture precisely the absolute intensity dynamics for EGFP-NEMO at each single spot. Therefore, to directly model the relative effects of basal and transcriptional feedback, we used three main variables. First, we defined the intensity of a spot (I) to represent a continuous approximation for ubiquitin chain size and NEMO activity resulting from molecules recruited at that spot. Second, we defined a variable X_basal for each individual spot as a proxy for feedback due to activity from basal DUBs expressed in resting cells. We modeled the X_basal variable such that the basal feedback increases as the corresponding NEMO spot grows through proportionate recruitment of DUB molecules on the same complex. Third, we defined a variable X_trnsxl to capture the transcriptional feedback due to the aggregate activity of all NEMO spots. Here, transcription-induced DUBs act in the same way as basal DUB molecules.

The model corresponding to N number of NEMO spots consists of 2N+1 ODEs: N for the individual spot intensities (I_i), N for the basal feedback variables corresponding to each spot (X_basal_i) and one for the transcriptional feedback variable (X_trnsxl). For each simulation, we modeled 200 single spots that form at regular intervals to approximate the response of a single cell to cytokine stimulation.

$$\frac{d[I_i]}{dt} = P_{form} * P_{bound} \frac{K_{growth}}{K_{limit} + [I_i]} - Kd_{basal} * Xlbasal_i * [I_i] - Kd_{trnsxl} * Xtrnsxl * [I_i]$$

$$\frac{d[X_basal_i]}{dt} = Kx_{basal} * [I_i] - Kxd_{basal} * [Xbasal_i]$$

$$\frac{d[X_trnsxl]}{dt} = Kx_{trnsxl} * \sum_i [I_i] - Kxd_{trnsxl} * [Xtrnsxl]$$

The variables and parameters in the model are as described in the following tables. We examined the relative effects of the two kinds of feedbacks by varying the parameters Kx_{basal} and Kx_{trnsxl}, which respectively control the amount of local and global feedback, by two orders of magnitudes (Figure S5A).

Variables used in the HyDeS model for NEMO spot intensity:

Variable Name	Description
$\boldsymbol{I_i}$	Intensity of 'i'th spot, proxy for NEMO recruitment at that spot
$\boldsymbol{X_basal_i}$	Basal feedback variable corresponding to 'i'th spot, proxy for feedback through basal/local DUB activity
$\boldsymbol{X_trnsxl}$	Transcriptional feedback variable, proxy for feedback through aggregate activity of all NEMO spots

Parameters used in the HyDeS model of NEMO spot intensity:

Parameter	Description	Default value
$\boldsymbol{P_{form}}$	Probability that the spot is formed as a function of time. Once formed, the spot is assumed to stay active.	Modeled as uniform distribution i.e. N spots form at regular intervals during the modeling time scale.
$\boldsymbol{P_{bound}}$	Probably that the ligand stays bound to the receptor and the complex is actively recruiting NEMO.	0.9
$\boldsymbol{K_{growth}}$	Michaelis-Menton like intrinsic rate of Ub polymerization	$1.12*10^{-7}$
$\boldsymbol{K_{limit}}$	Michaelis-Menton like kinetic constant to limit intrinsic polymerization with increasing spot intensity	0.1
$\boldsymbol{Kd_{basal}}$	Rate of basal feedback activity on individual spots	0.032
$\boldsymbol{Kd_{trnsxl}}$	Rate of transcriptional feedback activity on individual spots	0.08
$\boldsymbol{Kx_{basal}}$	Rate of activation of basal feedback due to Ub polymerization and DUB	23.3

	recruitment at the given spot	
$\boldsymbol{Kxd_{basal}}$	Decay rate of basal feedback	$8.7*10^{-4}$
$\boldsymbol{Kx_{trnsxl}}$	Rate of activation of transcriptional feedback due to collective activity of all NEMO spots	0.08
$\boldsymbol{Kxd_{trnsxl}}$	Decay rate of transcriptional feedback	$1.5*10^{-5}$

Variable-gain Stochastic Pooling Network model

Stochastic pooling networks (SPN) are a model sensory system in which noisy detectors are used to make independent and compressed measurements of a signal (McDonnell, 2009). These measurements are then pooled to average out the uncorrelated noise and reconstruct the original signal. Here we characterize a SPN system with the decoration of variable-gain (VG-SPN). In the VG-SPN system, each detector amplifies its binary measurement with a 'Gain' before pooling. Thus, the VG-SPN can have different configurations depending on the number of detectors and the Gain per detector. In the context of cytokine signaling mediated by CI complexes, each complex acts as a binary detector of the extracellular cytokine presence and the number of NEMO molecules recruited by a complex is considered its corresponding Gain. Therefore, we define two fundamental variables in our model of VG-SPN system. First, CI_{max} is the number of detectors in a VG-SPN configuration which is given by the maximum number of CI complexes that can form in a cell at saturation. Second, Gain is the number of NEMO molecules recruited at a given CI complex over the time course of its activity.

Depending on CI_{max} and Gain configurations, VG-SPN systems will have different maximum response (R_{max}) in terms of total number of NEMO molecules recruited. To systematically examine the noise mitigation properties of different VG-SPN configurations, we used a mathematically controlled approach by assuming each

configuration is capable of producing the same steady state response (Figure 7A). We therefore fixed the value of R_{max} and defined the Gain per complex to be inversely proportional to the maximum number of complexes as: Gain = R_{max}/CI_{max}. We then varied CI_{max} across orders of magnitude and calculated the noise associated with each configuration (Figure 7B).

The detector shot noise is the fraction of NEMO molecules recruited when a CI complex forms erroneously i.e. in absence of the signal. We assigned the probability of a complex to erroneously form as the 'shot noise level' (SNL). Therefore, the noise propagated when the SNL is less than the uniform probability ($1/CI_{max}$) will correspond to one complex forming erroneously which, in turn, will be the Gain associated with that configuration. For example, erroneous activation of a 1-receptor system via shot noise will activate the system to its fullest capabilities. Due to the inverse correlation of CI_{max} with Gain, the shot noise will decrease with CI_{max} (Figure 7B, top). However, after reaching a certain value of CI_{max}, the SNL will become higher than the uniform probability allowing more than one complexes to erroneously form at the same time. Configurations beyond such value of CI_{max} will hit the noise floor and the shot noise will not decrease further.

$$Fractional\ Shot\ Noise = \begin{cases} \dfrac{Gain}{R_{max}} = \dfrac{1}{CI_{max}}, & when\ SNL < \dfrac{1}{CI_{max}} \\ \dfrac{SNL * CI_{max} * Gain}{R_{max}} = SNL, & when\ SNL > \dfrac{1}{CI_{max}} \end{cases}$$

We observed considerable variability in intensities of NEMO complexes formed in response to a particular cytokine (Figures 2D, 5C, D). This variability suggests that although the mean value of Gain per complex is cytokine specific, the gain associated with a single complex can vary among different complexes within a cell, and these differences will introduce 'Gain noise' in the pooled response. Specifically, Gain noise

captures the noise in the pooled response corresponding to same number of active detector complexes due the variability in Gain per complex (i.e. the number of NEMO molecules recruited to a single complex over its lifespan). We examined the effect of different VG-SPN configurations on the Gain noise using the mathematically controlled approached as described earlier. We modeled the Gain per complex with Gaussian distribution and using the coefficient of variation given by the 'Gain noise level' (GNL) as: σ_G = GNL*Gain. Therefore, for a given VG-SPN configuration, each cell will have a response corresponding to the sum of CI_{max} random numbers obtained from the distribution $\mathcal{N}(Gain, \sigma_G)$. We simulated 1000 cells for every configuration with different GNL values and calculated the Gain noise (coefficient of variation) that contribute to the resulting responses (Figure 7B, bottom).

Next, we developed a computational VG-SPN model to generate simulated data for channel capacity calculations using the framework developed by (Selimkhanov et al., 2014) and codes from our previous study (Zhang et al., 2017). In this model, the signal S in the range (0,1] represents the extracellular cytokine dose where S=1 corresponds to saturating dose. The dose range is equally divided in discrete levels controlled by the hyperparameter 'numDoses'.

$$S_i \in (0,1]\,, i \in [1, numDoses]$$

For each input signal S_i, we simulate responses from N cells, where N is another hyperparameter. The response of jth cell to ith level of input signal (R_{ij}) is a scalar quantity representing the total number of recruited NEMO molecules. The model thus produces simulated data as response vectors of length N for each of the 'numDoses' number of input conditions. The data workflow is as follows:

$$S = \begin{bmatrix} S_1 \\ S_2 \\ \vdots \\ S_i \\ \vdots \\ S_{numDoses} \end{bmatrix} \rightarrow R = \begin{bmatrix} R_1 \\ R_2 \\ \vdots \\ R_i \\ \vdots \\ R_{numDoses} \end{bmatrix} where\ S_i \rightarrow R_i = [R_{i1} \quad R_{i2} \quad \dots \quad R_{ij} \quad \dots \quad R_{iN}]$$

As described earlier, CI_{max} is the maximum number of NEMO complexes a cell can form at saturating conditions i.e. when $S_i = 1$. CI_{max} will be related to the number of surface receptors (SR) per cell through the cytokine-dependent valency as: CI_{max} = SR/valency. Therefore, to model cell-to-cell variability in receptor expression (Figure 1B), we assumed that CI_{max} follows a Gaussian distribution over the N simulated cells with coefficient of variation given by the Receptor Noise Level (RNL).

$$CI_{max_j} \sim \mathcal{N}(CI_{max}, RNL * CI_{max})$$

Here the mean CI_{max} is set by the VG-SPN configuration and RNL is another hyperparameter controlling the coefficient of variation in receptor expression. For instance, for N=1000, CI_{max}=100 and RNL=0.3, we sample 1000 normally distributed integer random numbers from $\mathcal{N}(100,30)$ to simulate responses for 1000 cells where each cell can maximally form around 100 complexes with coefficient of variation 0.3.

We used binomial distribution to model switch-like properties of complex formation in the detection and switching steps (Figure 6A) wherein the probability of complex formation (P_{form}) increases with the input signal S_i. We used modified Hill function to relate S_i with P_{form} (Figure 2F).

$$CI^*_{max_j} \sim Binomial\left(CI_{max_j}, P_{form}\right), \qquad where \quad P_{form} = \frac{(1+0.5) * S_i^3}{0.5 + S_i^3}$$

Here $CI^*_{max_j}$ is the number of complexes formed in response to the dose level S_i in a cell having capacity to form CI_{max_j} complexes at saturation. Therefore, for a given ‘j’th cell,

we generate CI_{max_j} random numbers between [0,1]. We then check how many of those fall below the P_{form} value corresponding to the given signal S_i. This number, $CI^*_{max_j}$, will be used as number of active complexes in the 'j'th cell. Thus, the output of detection step corresponding to signal S_i is the following vector:

$$S_i \rightarrow \left[CI^*_{max_1} \quad CI^*_{max_2} \quad \dots \quad CI^*_{max_j} \quad \dots \quad CI^*_{max_{N^\#}}\right]$$

Note that $N^\# \leq N$ because for lower doses there might be some cells that don't cross the P_{form} threshold i.e. they don't form any spots.

In the detection step, we simulated the number of complexes formed by a given cell ($CI^*_{max_j}$) in response to a given dose (S_i). Next, in the amplification step (Figure 6A), we model the Gain (G_k) in terms of number of NEMO molecules recruited per complex. The response of a cell i.e. total number of recruited NEMO molecules is then sum of the Gains associated with all the complexes formed in that cell (signal pooling step, Figure 6A).

$$Response\ R\left(S_i, CI_{max_j}\right) = \sum_{k=1}^{CI^*_{max_j}} G_k$$

We assume a linear relation between Gain per complex (in terms of NEMO molecules) and the experimentally observed integrated intensity (AUC_i, Figure S5).

$$G_k(NEMO\ Molecules) = AUCi_to_NEMO_factor * G_k(Intensity)$$

Here AUCi_to_NEMO_factor is another hyperparameter. As previously stated for calculation of Gain noise, we use Gaussian distribution to model the variability in G_k within a cell.

$$G_k \sim \mathcal{N}(Gain, GNL * Gain)$$

Here GNL is the Gain Noise Level i.e. the coefficient of variation of Gains corresponding

to different complexes within a cell. We use the quadratic relation between intracellular mean and variance of AUC_i (Figure S4E) to get GNL for different mean values of Gain corresponding to different VG-SPN configurations.

To summarize, response of 'j'th cell with a VG-SPN configuration given by (CI_{max}, Gain) to the input signal level S_i is calculated as following:

$$Response\ R_{ij}(S_i, CI_{max}, Gain) = \sum_{k=1}^{CI^*_{max_j}} AUCi_to_NEMO_factor * \mathcal{N}(Gain, GNL * Gain)_k$$

$$Where \qquad CI^*_{max_j} = Count(CI_{max_j} < P_{form}(S_i))$$

$$And \qquad CI_{max_j} \sim \mathcal{N}(CI_{max}, RNL * CI_{max})$$

This process is repeated for N number of cells and 'numDoses' number of input signal levels:

$$CI_{max_j} \in [CI_{max_1} \quad CI_{max_2} \quad \dots \quad CI_{max_N}]$$

$$S_i \in [S_1 \quad S_2 \quad \dots \quad S_{numDoses}]$$

There are two independent variables in this model, CI_{max} and Gain, which completely define the VG-SPN configuration. In other words, the model allows independent 'tuning' of maximum number of NEMO complexes (i.e. number of surface receptors) and the Gain (i.e. number of NEMO recruited by each complex) to achieve a certain channel capacity.

The model has four hyperparameters: numDoses (controlling number of discrete dose levels), N (number of cells to simulate per dose level), RNL (coefficient of variation in CI_{max} over cells) and AUCi_to_NEMO_factor (relating integrated intensity to number of NEMO molecules per complex). In addition to these four, the channel capacity calculation framework developed by (Selimkhanov et al., 2014) requires another hyperparameter 'K' which controls the K-nn classification to estimate probability densities of response given

input dose level. To interface the VG-SPN model with our previous code for channel capacity calculations (Zhang et al., 2017), we adjusted these five hyperparameters to avoid technical biases that can artificially limit calculated channel capacity values for a VG-SPN configuration.

After running preliminary computational experiments, we arrived at a set of values for the five hyperparameters. Then, for each hyperparameter, we varied its value while keeping other values in the set constant to confirm that the chosen value doesn't limit the maximum channel capacity value of a VG-SPN configuration. By iterating through this process several times, and repeating it for multiple values of Rmax, we converged on the following settings (Figure S7A).

First, the number of simulated input conditions can artificially limit the channel capacity calculated for a signaling system, but becomes increasingly costly to compute when input conditions become excessively high. We simulated our model with 10, 30, 60 and 100 input conditions ('numDoses' parameter in the methods) and found that the max channel capacity does not increase beyond 60. Next, we observed that the max channel capacity decreases as the cell-to-cell variability in number of CI per cell (RNL parameter) increases. We therefore chose the intermediate value of stdR = 0.3 that is consistent with our FACS receptor analysis (Figs. 1 and S1). Next, the value of K used for K-NN classification introduces minial bias beyond a value of 5 and contributes to computational cost at higher values. We therefore chose K = 5, consistent with previous calculations (Selimkhanov et al., 2014). We then found that simulating more than 1000 cells per input condition does not increase the channel capacity but significantly affects simulation time, so we chose N = 1000. Finally, in order to relate amplifier gain (G_L) to the quadratic noise

relationship observed in data (Figure S4E), we estimated the factor to convert integrated spot intensity to number of NEMO molecules at a CI-like complex ('AUCi_to_NEMO_factor'). Values for the conversion factor did not have significant effects on max channel capacity beyond a value of 200.

Once we fixed the hyperparameters of the model, we removed the constraints of the mathematically controlled framework and allowed the two model variables, CI_{max} and Gain, to vary independently. We then calculated the channel capacities corresponding to VG-SPN configurations given by different (CI_{max}, Gain) pairs using previous codes (Zhang et al., 2017) which are based on the framework developed by (Selimkhanov et al., 2014). We also calculated the maximum response (R_{max}) corresponding to each (CI_{max}, G) configuration which is simply given by CI_{max}*Gain. Effectively, the value of R_{max} relates to the number of NEMO or other response molecules in the cytoplasm that can be activated by a VG-SPN configuration.

Variables used in the VG-SPN model:

Variable	**Description**	**Formula**
CI_{max}	Maximum number of CI complexes that a cell can form at saturation	Independent variable
Gain	Number of NEMO molecules recruited by a CI complex	Independent variable
$\boldsymbol{CI_{max_j}}$	CI_{max} corresponding to 'j'th cell	$CI_{max_j} \sim \mathcal{N}(CI_{max}, RNL * CI_{max})$
P_{form}	Probability of complex formation as a function of input dose level S_i	$P_{form} = \frac{(1+0.5) * S_i^3}{0.5 + S_i^3}$
$\boldsymbol{CI^*_{max_j}}$	Number of CI complexes formed in response to a given input dose level in 'j'th cell	$CI^*_{max_j} \sim Binomial\left(CI_{max_j}, P_{form}\right)$
G_k	Gain associated with 'k'th complex within a cell	$G_k \sim \mathcal{N}(Gain, GNL * Gain)$
GNL	Coefficient of variation of Gains associated with different CI complexes within a cell	GNL = 0.495*Gain^2 – 0.096*Gain + 0.05 (where Gain is in terms of AUC_i)

Hyperparameters used in the VG-SPN model:

Hyperparameter	Description	Value
numDoses	Number of discrete input dose levels used to simulate the model response	60
N	Number of cells simulated for each input dose level	1000
RNL	Receptor noise level in terms of coefficient of variation in CI_{max} across cells	0.3
AUC_i_to_NEMO_factor	Factor to convert integrated intensity (AUCi) of observed CI spots into number of NEMO molecules recruited at that complex	200
K	Value of K used for K-nn classification in the framework developed by (Selimkhanov et al., 2014)	5

Statistical Analyses

Distributions of physical properties of NEMO puncta were compared to see if they were statistically different from one another (Figure 2C). The distributions were compared with a student's t-test (using native MATLAB functions), yielding p-values for the null hypothesis that the two distributions were from the same (normal) distribution, with identical means and standard deviations. Each null hypothesis was rejected at the 5 percent significance level with p-values $<< 10^{-20}$ for every TNF and IL-1 pair with the same dosage condition.

Spearman's rank correlation and linear regression were performed on NEMO predictors for the RELA responses (and the log-transformed predictors/responses) for cells responding to TNF and IL-1. Native MATLAB functions were used to calculate all coefficients. Multiple linear regression was also performed on NEMO predictors for RELA AUC-Fold response in cells responding to TNF and IL-1 to see whether combinations of descriptors improve R^2 values. R^2 values shown in Figure S3C are the best R^2 determined for the indicated number of predictors when considering all possible predictor

combinations. Combination of predictors provided only marginal improvements, with maximum R^2 values approaching 0.7 and 0.8 for the linear and log-transformed (respectively).

References:

Adamson, A., Boddington, C., Downton, P., Rowe, W., Bagnall, J., Lam, C., Maya-Mendoza, A., Schmidt, L., Harper, C.V., Spiller, D.G.*, et al.* (2016). Signal transduction controls heterogeneous NF-kappaB dynamics and target gene expression through cytokine-specific refractory states. Nat Commun *7*, 12057.

Aggarwal, B.B. (2003). Signalling pathways of the TNF superfamily: a double-edged sword. Nat Rev Immunol *3*, 745-756.

Ahmad, R., Sylvester, J., and Zafarullah, M. (2007). MyD88, IRAK1 and TRAF6 knockdown in human chondrocytes inhibits interleukin-1-induced matrix metalloproteinase-13 gene expression and promoter activity by impairing MAP kinase activation. Cell Signal *19*, 2549-2557.

Alon, U. (2007). An introduction to systems biology : design principles of biological circuits (Boca Raton, FL: Chapman & Hall/CRC).

Ashall, L., Horton, C.A., Nelson, D.E., Paszek, P., Harper, C.V., Sillitoe, K., Ryan, S., Spiller, D.G., Unitt, J.F., Broomhead, D.S.*, et al.* (2009). Pulsatile stimulation determines timing and specificity of NF-kappaB-dependent transcription. Science *324*, 242-246.

Bebes, A., Kovács-Sólyom, F., Prihoda, J., Kui, R., Kemény, L., and Gyulai, R. (2014). Interleukin-1 receptors are differentially expressed in normal and psoriatic T cells. Mediators Inflamm *2014*, 472625-472625.

Berg, H.C., and Purcell, E.M. (1977). Physics of chemoreception. Biophys J *20*, 193-219.

Besse, A., Lamothe, B., Campos, A.D., Webster, W.K., Maddineni, U., Lin, S.-C., Wu, H., and Darnay, B.G. (2007). TAK1-dependent signaling requires functional interaction with TAB2/TAB3. The Journal of Biological Chemistry *282*, 3918-3928.

Bryl, E., Vallejo, A.N., Matteson, E.L., Witkowski, J.M., Weyand, C.M., and Goronzy, J.J. (2005). Modulation of CD28 expression with anti-tumor necrosis factor alpha therapy in rheumatoid arthritis. Arthritis Rheum *52*, 2996-3003.

Cheong, R., Rhee, A., Wang, C.J., Nemenman, I., and Levchenko, A. (2011). Information transduction capacity of noisy biochemical signaling networks. Science *334*, 354-358.

Clague, M.J., Urbe, S., and Komander, D. (2019). Breaking the chains: deubiquitylating enzyme specificity begets function. Nat Rev Mol Cell Biol *20*, 338-352.

Clark, K., Nanda, S., and Cohen, P. (2013). Molecular control of the NEMO family of ubiquitin-binding proteins. Nat Rev Mol Cell Biol *14*, 673-685.

Dower, S.K., Kronheim, S.R., March, C.J., Conlon, P.J., Hopp, T.P., Gillis, S., and Urdal, D.L. (1985). Detection and characterization of high affinity plasma membrane receptors for human interleukin 1. J Exp Med *162*, 501-515.

Ea, C.K., Deng, L., Xia, Z.P., Pineda, G., and Chen, Z.J. (2006). Activation of IKK by TNFalpha requires site-specific ubiquitination of RIP1 and polyubiquitin binding by NEMO. Mol Cell *22*, 245-257.

Grell, M., Wajant, H., Zimmermann, G., and Scheurich, P. (1998). The type 1 receptor (CD120a) is the high-affinity receptor for soluble tumor necrosis factor. Proc Natl Acad Sci U S A *95*, 570-575.

Haas, T.L., Emmerich, C.H., Gerlach, B., Schmukle, A.C., Cordier, S.M., Rieser, E., Feltham, R., Vince, J., Warnken, U., Wenger, T.*, et al.* (2009). Recruitment of the linear ubiquitin chain assembly complex stabilizes the TNF-R1 signaling complex and is required for TNF-mediated gene induction. Mol Cell *36*, 831-844.

Hayden, M.S., and Ghosh, S. (2008). Shared principles in NF-kappaB signaling. Cell *132*, 344-362.

Hinz, M., and Scheidereit, C. (2014). The IkappaB kinase complex in NF-kappaB regulation and beyond. EMBO Rep *15*, 46-61.

Hoffmann, A., Levchenko, A., Scott, M.L., and Baltimore, D. (2002). The IkappaB-NF-kappaB signaling module: temporal control and selective gene activation. Science *298*, 1241-1245.

Hwang, B., Phan, F.P., McCool, K., Choi, E.Y., You, J., Johnson, A., Audhya, A., and Miyamoto, S. (2015). Quantification of cellular NEMO content and its impact on NF-kappaB activation by genotoxic stress. PLoS One *10*, e0116374.

Ikeda, F., Deribe, Y.L., Skanland, S.S., Stieglitz, B., Grabbe, C., Franz-Wachtel, M., van Wijk, S.J., Goswami, P., Nagy, V., Terzic, J.*, et al.* (2011). SHARPIN forms a linear ubiquitin ligase complex regulating NF-kappaB activity and apoptosis. Nature *471*, 637-641.

Jackson-Bernitsas, D.G., Ichikawa, H., Takada, Y., Myers, J.N., Lin, X.L., Darnay, B.G., Chaturvedi, M.M., and Aggarwal, B.B. (2007). Evidence that TNF-TNFR1-TRADD-TRAF2-RIP-TAK1-IKK pathway mediates constitutive NF-kappaB activation and proliferation in human head and neck squamous cell carcinoma. Oncogene *26*, 1385-1397.

Jaqaman, K., Loerke, D., Mettlen, M., Kuwata, H., Grinstein, S., Schmid, S.L., and Danuser, G. (2008). Robust single-particle tracking in live-cell time-lapse sequences. Nat Methods *5*, 695-702.

Jupp, O.J., McFarlane, S.M., Anderson, H.M., Littlejohn, A.F., Mohamed, A.A., MacKay, R.H., Vandenabeele, P., and MacEwan, D.J. (2001). Type II tumour necrosis factor-

alpha receptor (TNFR2) activates c-Jun N-terminal kinase (JNK) but not mitogen-activated protein kinase (MAPK) or p38 MAPK pathways. Biochem J *359*, 525-535.

Karathanasis, C., Medler, J., Fricke, F., Smith, S., Malkusch, S., Widera, D., Fulda, S., Wajant, H., van Wijk, S.J.L., Dikic, I.*, et al.* (2020). Single-molecule imaging reveals the oligomeric state of functional TNFα-induced plasma membrane TNFR1 clusters in cells. Science Signaling *13*.

Komander, D., and Rape, M. (2012). The ubiquitin code. Annu Rev Biochem *81*, 203-229.

Kowalczyk, G.J., Cruz, J.A., Guo, Y., Zhang, Q., Sauerwald, N., and Lee, R.E.C. (2020). dNEMO: a tool for quantification of mRNA and punctate structures in time-lapse images of single cells. Bioinformatics.

Kull, F.C., Jacobs, S., and Cuatrecasas, P. (1985). Cellular receptor for 125I-labeled tumor necrosis factor: specific binding, affinity labeling, and relationship to sensitivity. Proceedings of the National Academy of Sciences of the United States of America *82*, 5756-5760.

Lamprecht, M.R., Sabatini, D.M., and Carpenter, A.E. (2007). CellProfiler: free, versatile software for automated biological image analysis. Biotechniques *42*, 71-75.

Lee, R.E., Walker, S.R., Savery, K., Frank, D.A., and Gaudet, S. (2014). Fold change of nuclear NF-kappaB determines TNF-induced transcription in single cells. Mol Cell *53*, 867-879.

Lehmann, V., and Droge, W. (1986). Demonstration of membrane receptors for human natural and recombinant 125I-labeled tumor necrosis factor on HeLa cell clones and their role in tumor cell sensitivity. Eur J Biochem *158*, 1-5.

Lim, R., Barker, G., and Lappas, M. (2017). TRADD, TRAF2, RIP1 and TAK1 are required for TNF-α-induced pro-labour mediators in human primary myometrial cells. Am J Reprod Immunol *78*.

Lin, S.C., Lo, Y.C., and Wu, H. (2010). Helical assembly in the MyD88-IRAK4-IRAK2 complex in TLR/IL-1R signalling. Nature *465*, 885-890.

Lipniacki, T., Puszynski, K., Paszek, P., Brasier, A.R., and Kimmel, M. (2007). Single TNFalpha trimers mediating NF-kappaB activation: stochastic robustness of NF-kappaB signaling. BMC Bioinformatics *8*, 376.

MacEwan, D.J. (2002). TNF ligands and receptors--a matter of life and death. Br J Pharmacol *135*, 855-875.

McDonnell, M.D. (2009). Information capacity of stochastic pooling networks is achieved by discrete inputs. Phys Rev E Stat Nonlin Soft Matter Phys *79*, 041107.

McDonnell, M.D., and Abbott, D. (2009). What is stochastic resonance? Definitions, misconceptions, debates, and its relevance to biology. PLoS Comput Biol *5*, e1000348.

Micheau, O., and Tschopp, J. (2003). Induction of TNF receptor I-mediated apoptosis via two sequential signaling complexes. Cell *114*, 181-190.

Mokashi, C.S., Schipper, D.L., Qasaimeh, M.A., and Lee, R.E.C. (2019). A System for Analog Control of Cell Culture Dynamics to Reveal Capabilities of Signaling Networks. iScience *19*, 586-596.

Nelson, D.E., Ihekwaba, A.E., Elliott, M., Johnson, J.R., Gibney, C.A., Foreman, B.E., Nelson, G., See, V., Horton, C.A., Spiller, D.G.*, et al.* (2004). Oscillations in NF-kappaB signaling control the dynamics of gene expression. Science *306*, 704-708.

Neumann, D., Kollewe, C., Martin, M.U., and Boraschi, D. (2000). The membrane form of the type II IL-1 receptor accounts for inhibitory function. J Immunol *165*, 3350-3357.

Pabon, N.A., Zhang, Q., Cruz, J.A., Schipper, D.L., Camacho, C.J., and Lee, R.E.C. (2019). A network-centric approach to drugging TNF-induced NF-kappaB signaling. Nat Commun *10*, 860.

Pahl, H.L. (1999). Activators and target genes of Rel/NF-kappaB transcription factors. Oncogene *18*, 6853-6866.

Purvis, J.E., and Lahav, G. (2013). Encoding and decoding cellular information through signaling dynamics. Cell *152*, 945-956.

Ran, F.A., Hsu, P.D., Wright, J., Agarwala, V., Scott, D.A., and Zhang, F. (2013). Genome engineering using the CRISPR-Cas9 system. Nature protocols *8*, 2281-2308.

Rubin, B.Y., Anderson, S.L., Sullivan, S.A., Williamson, B.D., Carswell, E.A., and Old, L.J. (1985). High affinity binding of 125I-labeled human tumor necrosis factor (LuKII) to specific cell surface receptors. J Exp Med *162*, 1099-1104.

Savageau, M.A. (1976). Biochemical systems analysis : a study of function and design in molecular biology (Reading, Mass.: Addison-Wesley Pub. Co., Advanced Book Program).

Scholefield, J., Henriques, R., Savulescu, A.F., Fontan, E., Boucharlat, A., Laplantine, E., Smahi, A., Israel, A., Agou, F., and Mhlanga, M.M. (2016). Super-resolution microscopy reveals a preformed NEMO lattice structure that is collapsed in incontinentia pigmenti. Nat Commun *7*, 12629.

Selimkhanov, J., Taylor, B., Yao, J., Pilko, A., Albeck, J., Hoffmann, A., Tsimring, L., and Wollman, R. (2014). Systems biology. Accurate information transmission through dynamic biochemical signaling networks. Science *346*, 1370-1373.

Serke, S., van Lessen, A., and Huhn, D. (1998). Quantitative fluorescence flow cytometry: a comparison of the three techniques for direct and indirect immunofluorescence. Cytometry *33*, 179-187.

Skaug, B., Chen, J., Du, F., He, J., Ma, A., and Chen, Z.J. (2011). Direct, noncatalytic mechanism of IKK inhibition by A20. Mol Cell *44*, 559-571.

Sumit, M., Jovic, A., Neubig, R.R., Takayama, S., and Linderman, J.J. (2019). A Two-Pulse Cellular Stimulation Test Elucidates Variability and Mechanisms in Signaling Pathways. Biophys J *116*, 962-973.

Tarantino, N., Tinevez, J.Y., Crowell, E.F., Boisson, B., Henriques, R., Mhlanga, M., Agou, F., Israel, A., and Laplantine, E. (2014). TNF and IL-1 exhibit distinct ubiquitin requirements for inducing NEMO-IKK supramolecular structures. J Cell Biol *204*, 231-245.

Tay, S., Hughey, J.J., Lee, T.K., Lipniacki, T., Quake, S.R., and Covert, M.W. (2010). Single-cell NF-kappaB dynamics reveal digital activation and analogue information processing. Nature *466*, 267-271.

Wang, C., Han, B., Zhou, R., and Zhuang, X. (2016). Real-Time Imaging of Translation on Single mRNA Transcripts in Live Cells. Cell *165*, 990-1001.

Watanabe, N., Kuriyama, H., Sone, H., Neda, H., Yamauchi, N., Maeda, M., and Niitsu, Y. (1988). Continuous internalization of tumor necrosis factor receptors in a human myosarcoma cell line. J Biol Chem *263*, 10262-10266.

Werner, S.L., Barken, D., and Hoffmann, A. (2005). Stimulus specificity of gene expression programs determined by temporal control of IKK activity. Science *309*, 1857-1861.

Werner, S.L., Kearns, J.D., Zadorozhnaya, V., Lynch, C., O'Dea, E., Boldin, M.P., Ma, A., Baltimore, D., and Hoffmann, A. (2008). Encoding NF-kappaB temporal control in response to TNF: distinct roles for the negative regulators IkappaBalpha and A20. Genes Dev *22*, 2093-2101.

Wertz, I.E., O'Rourke, K.M., Zhou, H., Eby, M., Aravind, L., Seshagiri, S., Wu, P., Wiesmann, C., Baker, R., Boone, D.L.*, et al.* (2004). De-ubiquitination and ubiquitin ligase domains of A20 downregulate NF-kappaB signalling. Nature *430*, 694-699.

Zhang, Q., Gupta, S., Schipper, D.L., Kowalczyk, G.J., Mancini, A.E., Faeder, J.R., and Lee, R.E.C. (2017). NF-κB Dynamics Discriminate between TNF Doses in Single Cells. Cell systems *5*, 638-645.e635.

Fig. 1

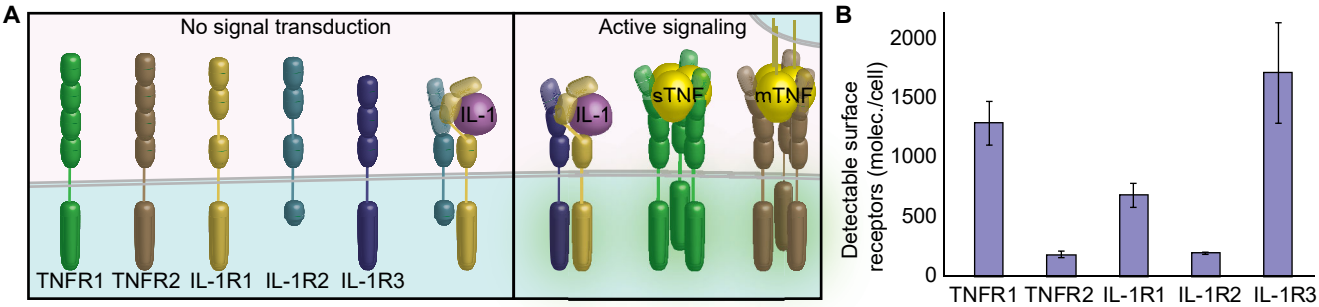
A
No signal transduction
Active signaling
IL-1
IL-1
sTNF
mTNF
TNFR1 TNFR2 IL-1R1 IL-1R2 IL-1R3
B
Detectable surface receptors (molec./cell)
2000
1500
1000
500
0
TNFR1 TNFR2 IL-1R1 IL-1R2 IL-1R3

Fig. 2

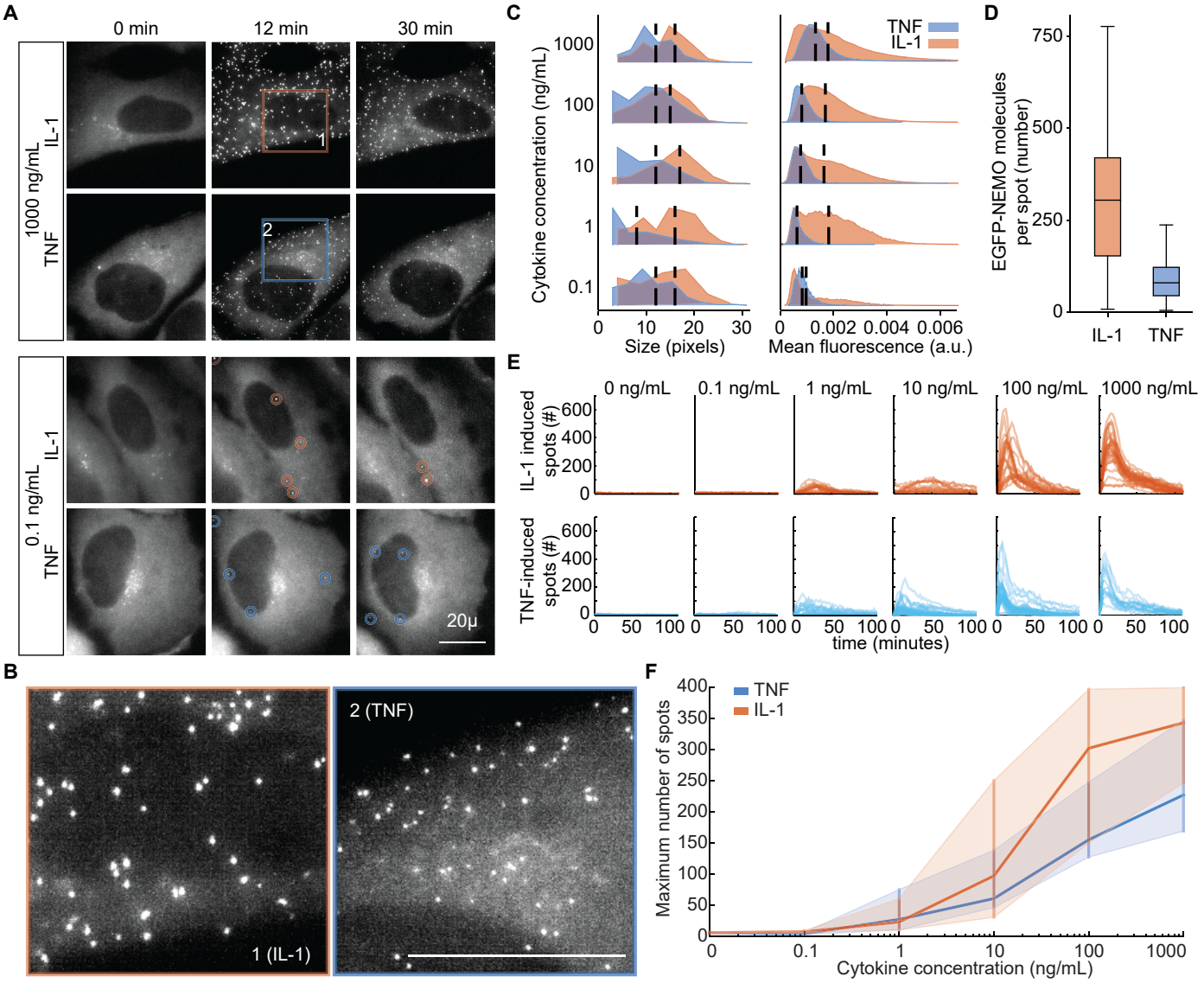
A
0 min
12 min
30 min
1000 ng/mL
IL-1
TNF
0.1 ng/mL
IL-1
TNF
1
2
20μ
B
1 (IL-1)
2 (TNF)
C
Cytokine concentration (ng/mL)
1000
100
10
1
0.1
TNF
IL-1
0
10
20
30
Size (pixels)
0
0.002
0.004
0.006
Mean fluorescence (a.u.)
D
EGFP-NEMO molecules per spot (number)
750
500
250
0
IL-1
TNF
E
0 ng/mL
0.1 ng/mL
1 ng/mL
10 ng/mL
100 ng/mL
1000 ng/mL
IL-1 induced spots (#)
TNF-induced spots (#)
600
400
200
0
0
50
100
time (minutes)
F
TNF
IL-1
Maximum number of spots
400
350
300
250
200
150
100
50
0
0
0.1
1
10
100
1000
Cytokine concentration (ng/mL)

Fig. 3

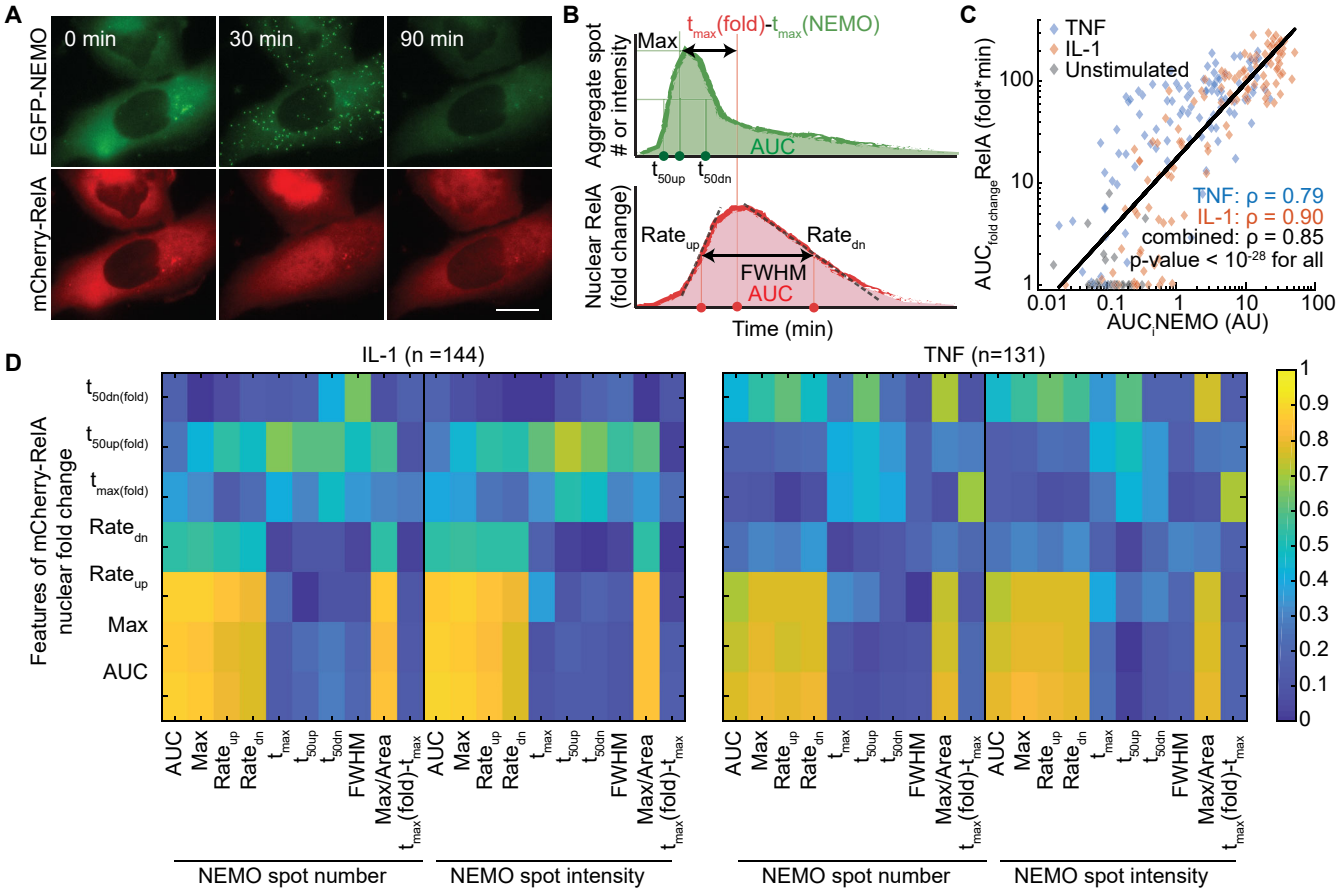
A
0 min
30 min
90 min
EGFP-NEMO
mCherry-RelA
B
Aggregate spot # or intensity
Max
t_{max}(fold)-t_{max}(NEMO)
AUC
t_{50up}
t_{50dn}
Nuclear RelA (fold change)
$Rate_{up}$
$Rate_{dn}$
FWHM
AUC
Time (min)
C
TNF
IL-1
Unstimulated
$AUC_{fold\ change}$ RelA (fold*min)
TNF: ρ = 0.79
IL-1: ρ = 0.90
combined: ρ = 0.85
p-value < 10^{-28} for all
AUC_{i}NEMO (AU)
D
IL-1 (n =144)
TNF (n=131)
Features of mCherry-RelA nuclear fold change
$t_{50dn(fold)}$
$t_{50up(fold)}$
$t_{max(fold)}$
$Rate_{dn}$
$Rate_{up}$
Max
AUC
AUC
Max
$Rate_{up}$
$Rate_{dn}$
t_{max}
t_{50up}
t_{50dn}
FWHM
Max/Area
t_{max}(fold)-t_{max}
NEMO spot number
NEMO spot intensity

Fig. 4

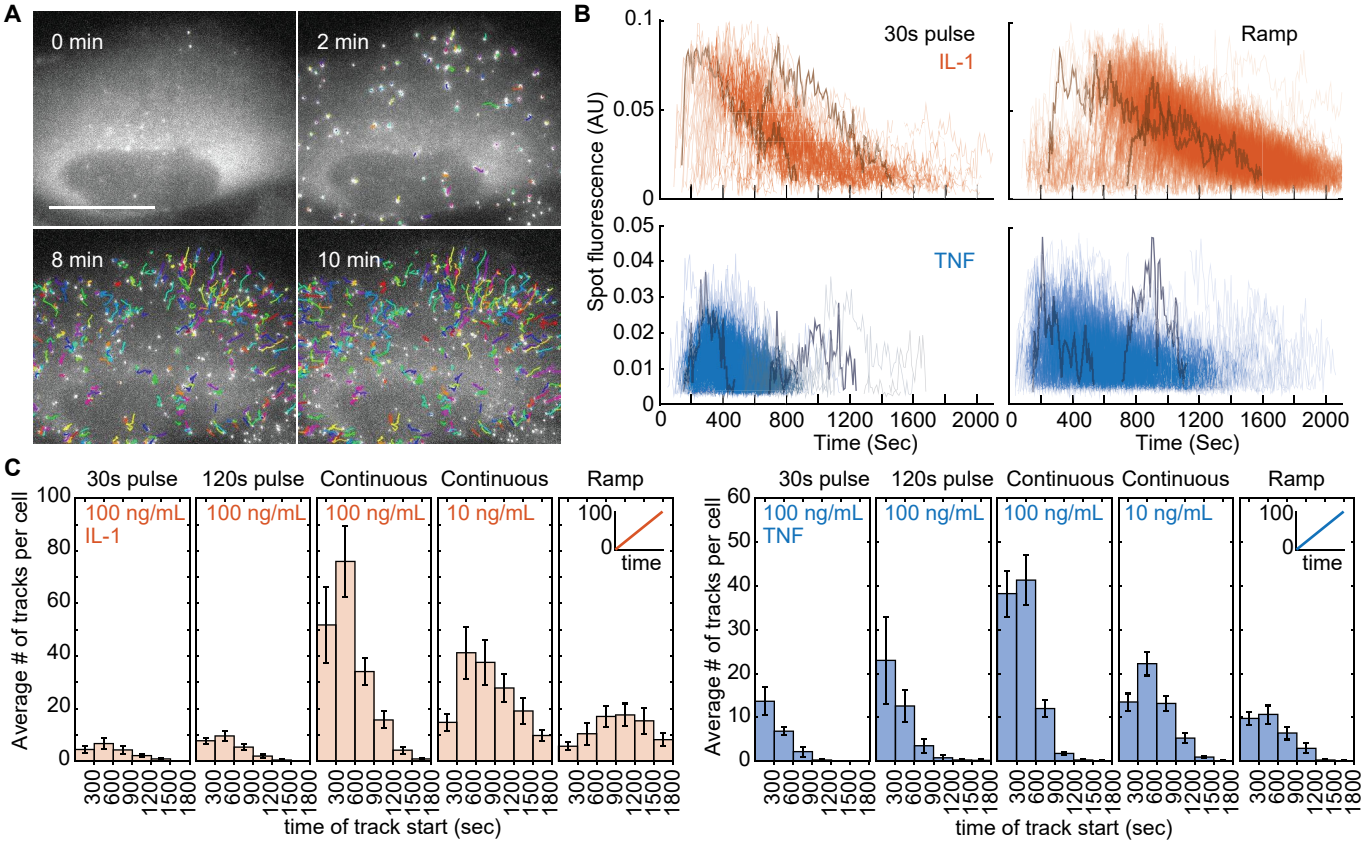
A
0 min
2 min
8 min
10 min
B
30s pulse
IL-1
Ramp
TNF
Spot fluorescence (AU)
Time (Sec)
C
30s pulse
120s pulse
Continuous
Continuous
Ramp
100 ng/mL
IL-1
10 ng/mL
time
Average # of tracks per cell
time of track start (sec)
TNF

Fig. 5

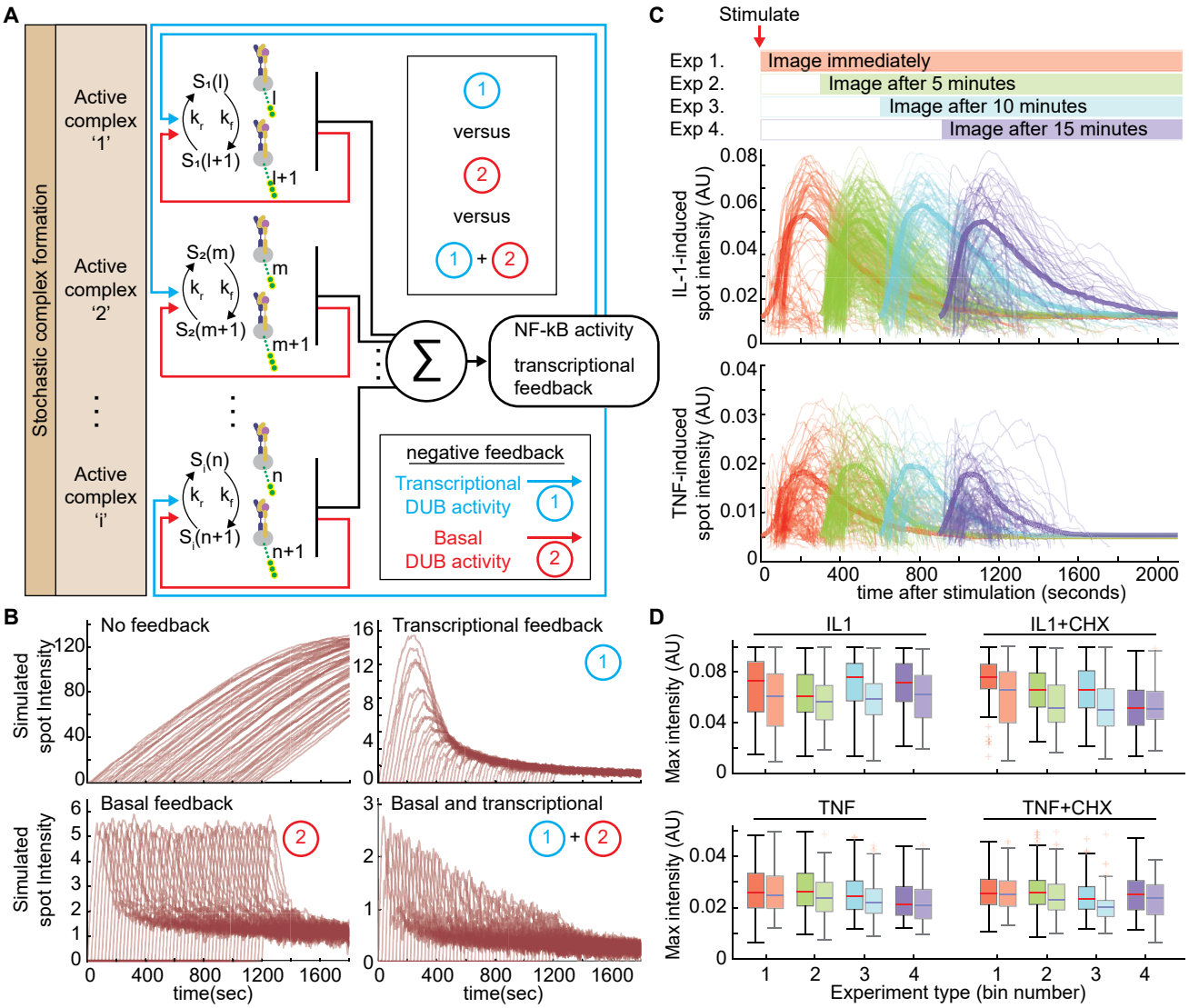
A
Stochastic complex formation
Active complex '1'
Active complex '2'
Active complex 'i'
versus
versus
NF-kB activity
transcriptional feedback
negative feedback
Transcriptional DUB activity
Basal DUB activity
B
No feedback
Transcriptional feedback
Basal feedback
Basal and transcriptional
Simulated spot Intensity
time(sec)
C
Stimulate
Exp 1. Image immediately
Exp 2. Image after 5 minutes
Exp 3. Image after 10 minutes
Exp 4. Image after 15 minutes
IL-1-induced spot intensity (AU)
TNF-induced spot intensity (AU)
time after stimulation (seconds)
D
IL1
IL1+CHX
TNF
TNF+CHX
Max intensity (AU)
Experiment type (bin number)

Fig. 6

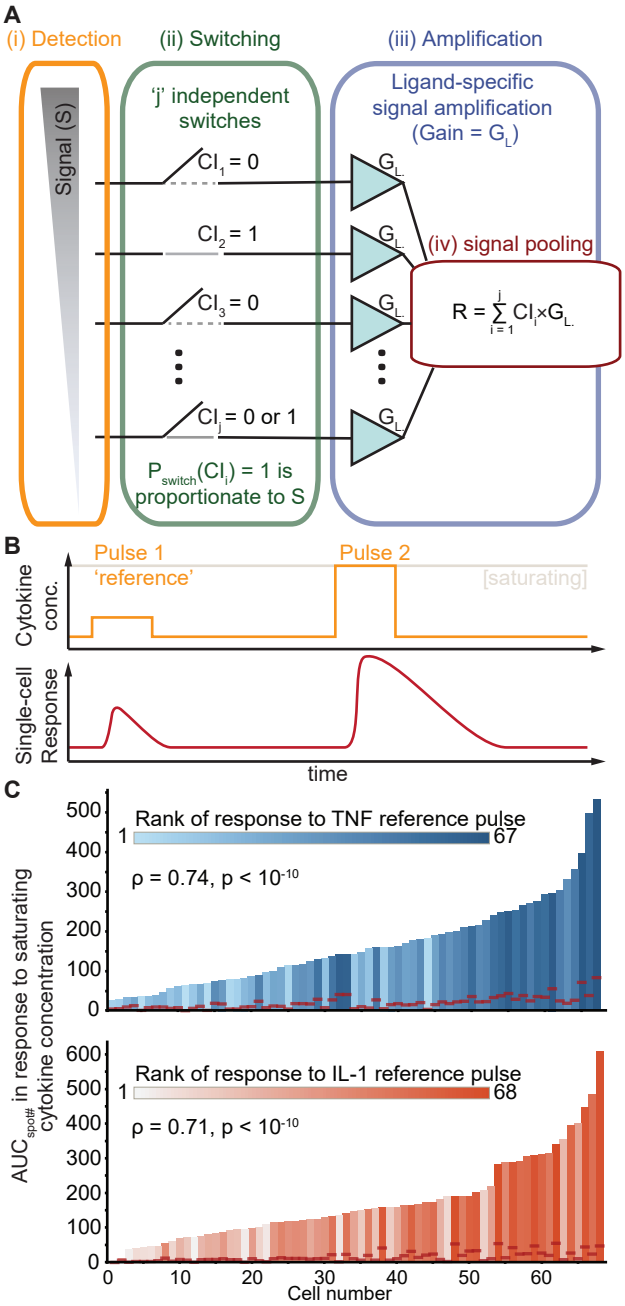
A
(i) Detection
(ii) Switching
(iii) Amplification
Signal (S)
'j' independent switches
Ligand-specific signal amplification (Gain = G_L)
$CI_1 = 0$
$CI_2 = 1$
$CI_3 = 0$
$CI_j = 0$ or 1
G_L
(iv) signal pooling
$R = \sum_{i=1}^{j} CI_i \times G_L$
$P_{switch}(CI_i) = 1$ is proportionate to S
B
Pulse 1
'reference'
Pulse 2
[saturating]
Cytokine conc.
Single-cell Response
time
C
Rank of response to TNF reference pulse
1
67
$\rho = 0.74$, $p < 10^{-10}$
Rank of response to IL-1 reference pulse
1
68
$\rho = 0.71$, $p < 10^{-10}$
$AUC_{spot\#}$ in response to saturating cytokine concentration
Cell number

Fig. 7

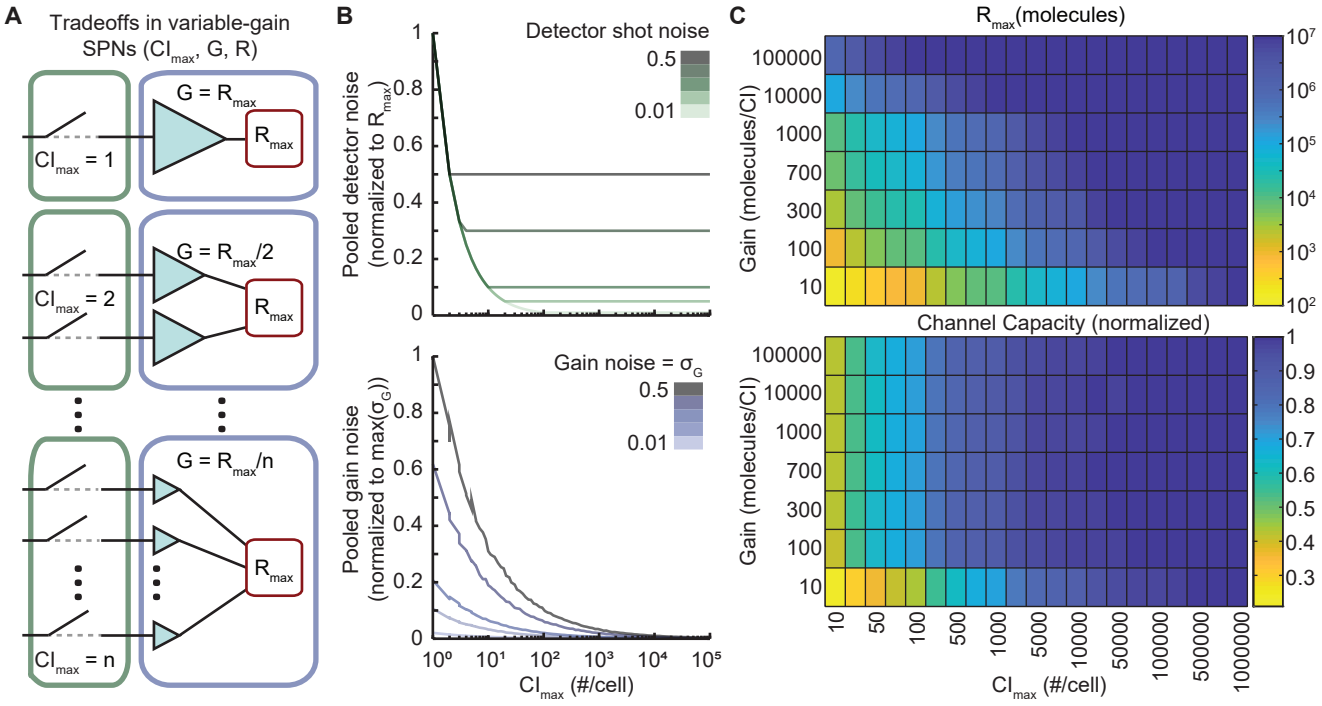
A
Tradeoffs in variable-gain SPNs (CI$_{max}$, G, R)
CI$_{max}$ = 1
G = R$_{max}$
R$_{max}$
CI$_{max}$ = 2
G = R$_{max}$/2
R$_{max}$
CI$_{max}$ = n
G = R$_{max}$/n
R$_{max}$
B
Detector shot noise
0.5
0.01
Pooled detector noise (normalized to R$_{max}$)
Gain noise = σ$_G$
0.5
0.01
Pooled gain noise (normalized to max(σ$_G$))
CI$_{max}$ (#/cell)
C
R$_{max}$(molecules)
Gain (molecules/CI)
Channel Capacity (normalized)
CI$_{max}$ (#/cell)